

JOINT INSTITUTE FOR AERONAUTICS AND ACOUSTICS

National Aeronautics and
Space Administration

Ames Research Center



Stanford University

JIAA TR - 109

An Aerodynamic Model for One and Two Degree of Freedom Wing Rock of Slender Delta Wings

By

GRANT
IN-02-CR
167896
P. 52

John Hong

Stanford University
Department of Aeronautics and Astronautics
Stanford, CA 94305

May 1993

(NASA-CR-193130) AN AERODYNAMIC
MODEL FOR ONE AND TWO DEGREE OF
FREEDOM WING ROCK OF SLENDER DELTA
WINGS (Stanford Univ.) 52 p

N93-27150

Unclas

G3/02 0167896

Abstract

The unsteady aerodynamic effects due to the separated flow around slender delta wings in motion have been analyzed using an extension of the Brown and Michael model, as first proposed by Arena. By combining the unsteady flow field solution with the rigid body Euler equations of motion, self-induced wing rock motion is simulated. The aerodynamic model successfully captures the qualitative characteristics of wing rock observed in experiments. For the one degree of freedom in roll case, the model is used to look into the mechanisms of wing rock and to investigate the effects of various parameters, like angle of attack, yaw angle, displacement of the separation point and wing inertia. To investigate the roll and yaw coupling for the delta wing, an additional degree of freedom is added. However, no limit cycle was observed in the two degree of freedom case. Nonetheless, the model can be used to apply various control laws to actively control wing rock using, for example, the displacement of the leading edge vortex separation point by inboard spanwise blowing.

PRECEDING PAGE BLANK NOT FILMED

100

Table of Contents

Abstract	2
Table of Contents.....	3
Table of Figures.....	4
Nomenclature.....	6
Introduction	9
Aerodynamic Model.....	9
Assumptions.....	9
Wing Geometry and Coordinate System	10
Complex Potential	12
Kutta Condition	15
Force Free Condition.....	15
Equations of Motion	18
Results and Discussion.....	21
One Degree of Freedom Wing Rock.....	21
Effect of Angle of Attack.....	22
Effect of Yaw Angle	23
Effect of Separation Point Displacement.....	24
Effect of Wing Inertia	25
Two Degree of Freedom Wing Rock	25
Conclusions.....	27
References	28
Figures.....	30

Table of Figures

Figure 1. Actual and Approximated Flow Fields	30
Figure 2. Schematic of the Delta Wing and Coordinate System.....	30
Figure 3. Sketch of Physical and Circle Plane	31
Figure 4. Flow Chart for Dynamic Simulation	31
Figure 5. Conceptual Stable and Unstable Roll Moment Trajectories	32
Figure 6(a). Wing Rock Time History ($\phi_0=0.5^\circ$, $\alpha=20^\circ$, $\beta=0^\circ$, $\epsilon=10^\circ$, $\delta=0\%$).....	32
Figure 6(b). Wing Rock Time History ($\phi_0=85^\circ$, $\alpha=20^\circ$, $\beta=0^\circ$, $\epsilon=10^\circ$, $\delta=0\%$)	33
Figure 7(a). Total Sectional Roll Moment Coefficient ($\alpha=20^\circ$, $\beta=0^\circ$, $\epsilon=10^\circ$, $\delta=0\%$).....	33
Figure 7(b). Top and Bottom Sectional Roll Moment Coefficient ($\alpha=20^\circ$, $\beta=0^\circ$, $\epsilon=10^\circ$, $\delta=0\%$).....	34
Figure 8(a). Spanwise Vortex Position During Wing Rock ($\alpha=20^\circ$, $\beta=0^\circ$, $\epsilon=10^\circ$, $\delta=0\%$).....	34
Figure 8(b). Normal Vortex Position During Wing Rock ($\alpha=20^\circ$, $\beta=0^\circ$, $\epsilon=10^\circ$, $\delta=0\%$).....	35
Figure 8(c). Unsteady Vortex Strength During Wing Rock ($\alpha=20^\circ$, $\beta=0^\circ$, $\epsilon=10^\circ$, $\delta=0\%$).....	35
Figure 9. Wing Rock Time History ($\phi_0=85^\circ$, $\alpha=10^\circ$, $\beta=0^\circ$, $\epsilon=10^\circ$, $\delta=0\%$).....	36
Figure 10(a). Total Sectional Roll Moment Coefficient ($\alpha=10^\circ$, $\beta=0^\circ$, $\epsilon=10^\circ$, $\delta=0\%$).....	36
Figure 10(b). Top and Bottom Sectional Roll Moment Coefficient ($\alpha=10^\circ$, $\beta=0^\circ$, $\epsilon=10^\circ$, $\delta=0\%$).....	37
Figure 11. Wing Rock Time History ($\phi_0=0.5^\circ$, $\alpha=30^\circ$, $\beta=0^\circ$, $\epsilon=10^\circ$, $\delta=0\%$).....	37
Figure 12(a). Total Sectional Roll Moment Coefficient ($\alpha=30^\circ$, $\beta=0^\circ$, $\epsilon=10^\circ$, $\delta=0\%$).....	38
Figure 12(b). Top and Bottom Sectional Roll Moment Coefficient ($\alpha=30^\circ$, $\beta=0^\circ$, $\epsilon=10^\circ$, $\delta=0\%$).....	38
Figure 13(a). Wing Rock Time History ($\phi_0=0.5^\circ$, $\alpha=20^\circ$, $\beta=5^\circ$, $\epsilon=10^\circ$, $\delta=0\%$).....	39
Figure 13(b). Wing Rock Time History ($\phi_0=85^\circ$, $\alpha=20^\circ$, $\beta=5^\circ$, $\epsilon=10^\circ$, $\delta=0\%$)	39
Figure 14(a). Total Sectional Roll Moment Coefficient ($\alpha=20^\circ$, $\beta=5^\circ$, $\epsilon=10^\circ$, $\delta=0\%$).....	40
Figure 14(b). Top and Bottom Sectional Roll Moment Coefficient ($\alpha=20^\circ$, $\beta=5^\circ$, $\epsilon=10^\circ$, $\delta=0\%$).....	40
Figure 15. Effective Angle of Attack, Yaw Angle and Semi-Apex Angle as a Function of Roll Angle for $\beta=0^\circ$ and $\beta=5^\circ$	41
Figure 16(a). Spanwise Vortex Position During Wing Rock ($\alpha=20^\circ$, $\beta=5^\circ$, $\epsilon=10^\circ$, $\delta=0\%$).....	42
Figure 16(b). Normal Vortex Position During Wing Rock ($\alpha=20^\circ$, $\beta=5^\circ$, $\epsilon=10^\circ$, $\delta=0\%$).....	42

Figure 16(c). Unsteady Vortex Strength During Wing Rock ($\alpha=20^\circ$, $\beta=5^\circ$, $\epsilon=10^\circ$, $\delta=0\%$).....	43
Figure 17(a). Wing Rock Time History ($\phi_0=0.5^\circ$, $\alpha=20^\circ$, $\beta=0^\circ$, $\epsilon=10^\circ$, $\delta l=0\%$, $\delta r=1\%$).....	43
Figure 17(b). Wing Rock Time History ($\phi_0=85^\circ$, $\alpha=20^\circ$, $\beta=0^\circ$, $\epsilon=10^\circ$, $\delta l=0\%$, $\delta r=1\%$).....	44
Figure 18(a). Total Sectional Roll Moment Coefficient ($\alpha=20^\circ$, $\beta=0^\circ$, $\epsilon=10^\circ$, $\delta l=0\%$, $\delta r=1\%$)	44
Figure 18(b). Top and Bottom Sectional Roll Moment Coefficient ($\alpha=20^\circ$, $\beta=0^\circ$, $\epsilon=10^\circ$, $\delta l=0\%$, $\delta r=1\%$).....	45
Figure 19(a). Spanwise Vortex Position During Wing Rock ($\alpha=20^\circ$, $\beta=0^\circ$, $\epsilon=10^\circ$, $\delta l=0\%$, $\delta r=1\%$)	45
Figure 19(b). Normal Vortex Position During Wing Rock ($\alpha=20^\circ$, $\beta=0^\circ$, $\epsilon=10^\circ$, $\delta l=0\%$, $\delta r=1\%$)	46
Figure 19(c). Unsteady Vortex Strength During Wing Rock ($\alpha=20^\circ$, $\beta=0^\circ$, $\epsilon=10^\circ$, $\delta l=0\%$, $\delta r=1\%$)	46
Figure 20(a). Effect of Inertia Variation on Wing Rock Amplitude ($\alpha=20^\circ$, $\beta=0^\circ$, $\epsilon=10^\circ$, $\delta=0\%$).....	47
Figure 20(b). Effect of Inertia Variation on Wing Rock Frequency ($\alpha=20^\circ$, $\beta=0^\circ$, $\epsilon=10^\circ$, $\delta=0\%$).....	47
Figure 21(a). Row and Yaw Euler Angle Time History ($\alpha=10^\circ$, $\beta=0^\circ$, $\epsilon=5^\circ$, $\delta=0\%$).....	48
Figure 21(b). Effective Angle of Attack, Yaw Angle and Roll Angle Time History ($\alpha=10^\circ$, $\beta=0^\circ$, $\epsilon=5^\circ$, $\delta=0\%$).....	48
Figure 22(a). Top and Bottom Sectional Roll Coefficient as a Function of Roll Angle ($\alpha=10^\circ$, $\beta=0^\circ$, $\epsilon=5^\circ$, $\delta=0\%$)	49
Figure 22(b). Top and Bottom Sectional Roll Coefficient as a Function of Yaw Angle ($\alpha=10^\circ$, $\beta=0^\circ$, $\epsilon=5^\circ$, $\delta=0\%$)	49
Figure 23(a). Spanwise Vortex Position as a Function of Roll Angle ($\alpha=10^\circ$, $\beta=0^\circ$, $\epsilon=5^\circ$, $\delta=0\%$).....	50
Figure 23(b). Normal Vortex Position as a Function of Roll Angle ($\alpha=10^\circ$, $\beta=0^\circ$, $\epsilon=5^\circ$, $\delta=0\%$).....	50
Figure 23(c). Unsteady Vortex Strength as a Function of Roll Angle ($\alpha=10^\circ$, $\beta=0^\circ$, $\epsilon=5^\circ$, $\delta=0\%$).....	51
Figure 24(a). Spanwise Vortex Position as a Function of Yaw Angle ($\alpha=10^\circ$, $\beta=0^\circ$, $\epsilon=5^\circ$, $\delta=0\%$).....	51
Figure 24(b). Normal Vortex Position as a Function of Yaw Angle ($\alpha=10^\circ$, $\beta=0^\circ$, $\epsilon=5^\circ$, $\delta=0\%$).....	52
Figure 24(c). Unsteady Vortex Strength as a Function of Yaw Angle ($\alpha=10^\circ$, $\beta=0^\circ$, $\epsilon=5^\circ$, $\delta=0\%$).....	52

Nomenclature

a	Local Semi-Span in Circle Plane
A	Wing Rock Amplitude
b	Trailing Edge Span
C	Rotation Matrix
C_p	Pressure Coefficient
C_r	Root Chord
C_{roll}	Sectional Roll Moment Coefficient
C_x	Rolling Moment Coefficient
C_y	Pitching Moment Coefficient
C_z	Yawing Moment Coefficient
E	Energy
F	Complex Potential, Force
g	Gravity
H^+	Source-Sink Sheet Strength per Unit Length
i	$\sqrt{-1}$
\bar{i}	Axial Unit Vector in Body Fixed Frame
I_{xx}	Moment of Inertia in Roll
I_{yy}	Moment of Inertia in Pitch
I_{zz}	Moment of Inertia in Yaw
\bar{j}	Axial Unit Vector in Ground Fixed Frame
\bar{j}	Spanwise Unit Vector in Body Fixed Frame
\bar{J}	Spanwise Unit Vector in Ground Fixed Frame
\bar{k}	Normal Unit Vector in Body Fixed Frame
\bar{K}	Normal Unit Vector in Ground Fixed Frame
M	External Moment

M_∞	Mach Number
p_∞	Freestream Static Pressure
s	Local Semi-Span of Wing
t	Time
u	Axial Component of Velocity
v	Spanwise Component of Velocity
V_∞	Freestream Velocity
w	Vertical Component of Velocity
W	Complex Velocity
x	Axial Body Fixed Coordinate in Physical Plane
y	Spanwise Body Fixed Coordinate in Physical Plane
z	Normal Body Fixed Coordinate in Physical Plane
α	Initial Angle of Attack
β	Initial Yaw Angle
δ	Separation Displacement from Leading Edge
ϵ	Semi-Apex Angle
ϕ	Euler Angle: Roll Like Rotation
γ	Initial Roll Angle
η	Euler Angle: Pitch Like Rotation
κ	Non-dimensional Circulation
λ	Location of Pivot Point on Wing
μ	Damping Coefficient
π	Pi
θ	Angular Coordinate in Circular Plane
ϑ	Temporary Integration Variable
ρ	Air Density
ρ_w	Wing Area Density

σ	Complex Coordinate in Physical Plane
ξ	Complex Coordinate in Circle Plane
ζ	Euler Angle: Yaw Like Rotation
Φ	Velocity Potential
Γ	Circulation
Ω	Angular Velocity
Ψ	Stream Function

Subscript

b	Body
c	Circle Plane
eff	Effective
l	Left
o	Initial
r	Body Fixed Frame, Right
R	Inertial Frame
s	Separation Point
t	Tangential
v	Vortex
w	Wing
∞	Freestream

INTRODUCTION

At high angles of attack the leeward flow field for slender delta wings is dominated by a highly organized vortical flow structure emanating from the sharp leading edges. The vortex sheet shed from the leading edge rolls up into a pair of strong vortices. As the angle of attack is increased, these leading edge vortices interact with each other and the wing itself, to create a sustained and large amplitude rigid body oscillation called wing rock. Such oscillations lead to a significant loss in lift and can present a serious safety problem during maneuvers, such as in landing. The maneuvering envelope of an aircraft exhibiting this behavior is also seriously restricted because the maximum incidence angle is often limited by the onset of wing rock before the occurrence of stall.

In recent years, the effectiveness of active control to alleviate this problem has been explored at the Stanford low speed wind tunnel. Wong^[18] has demonstrated that one degree of freedom wing rock can be suppressed by using tangential blowing as a roll control actuator and Pedreiro^[15] is examining the roll and yaw coupling for two degree of freedom wing rock and its elimination. However, the development of efficient control techniques and algorithms is constrained by the limited understanding of the basic aerodynamic mechanism and effect of various parameters on this phenomenon. This information must be understood so that wing rock may be avoided through design or efficiently controlled by active means. Also, due to the various conditions involved in the wing rock experiments, one lacks a general aerodynamic model where control laws can be tested for various configurations before actual implementation. These were the motivations for developing the following aerodynamic model.

Aerodynamic Model

Assumptions

An aerodynamic model is needed to obtain a fast estimate of the velocity and pressure fields around a delta wing which when combined with the equations of motion will capture wing rock. The vortex model for the vortical flow around the delta wing, first suggested by Brown and Michael^[4] and later expanded to the unsteady case by Arena^[1] is adequate for this purpose and is chosen to investigate the characteristics of wing rock. The model developed is an extension of the Arena model in the sense that for the one degree of freedom case parameters such as sideslip and displacement of the separation

oint were added and yaw motion in the plane of the wing i.e., an additional degree of freedom was included.

The actual flow field around the wing is illustrated in figure 1(a). In the model, separated flow on the delta wing is represented by a pair of line vortices connected to the leading edge by a straight vortex feeding sheet, as shown in figure 1(b). It has been shown experimentally^[17], that most of the axial vorticity of the leading edge vortex is confined to a viscous core region having a diameter of the order of 5% of the local semi-span. This fact justifies using a model where all the leading edge vortex vorticity is concentrated into two single line vortices.

Usually aircraft operate in the range of high Reynolds number, where the viscous effects are confined to very thin boundary layers along the surfaces and free shear layers in the fluid. Thus, it will be assumed that the only role of viscosity is to provide the mechanism for flow separation. It will also be understood that the Mach numbers to be used are sufficiently low to assume incompressible flow.

The present model does not predict vortex breakdown and no attempt is made to include this phenomena. Wing rock is observed at angles of attack where vortex breakdown does not occur^[2] and therefore the dynamic simulations will be applied at incidence angles where vortex breakdown does not affect the aerodynamics of the wing. The steep pressure gradient between the minimum pressure and the primary separation line causes an additional flow separation, which usually takes the form of a small secondary vortex. The effect of the secondary vortex on wing rock is small and will not be considered. It will also be assumed that the flow field is conical. The conical assumption requires that the wing geometry be conical and therefore all physical quantities are constant along rays emanating from the wing vertex. For a finite delta wing, subsonic conicality is an approximation that stems from ignoring the singular nature of the apex and the trailing edge effects. Nonetheless, it has been observed that the subsonic flow past a delta wing is approximately conical in a region downstream of the apex and upstream of the trailing edge. Later a slender body assumption will be used to simplify the governing equations.

Wing Geometry and Coordinate System

The unsteady aerodynamics of an aircraft maneuvering at high angles of attack are very configuration dependent. Therefore, to provide some insight into the unsteady aerodynamics, we will look into a simple configuration to effectively eliminate any configuration effects, namely that of a plain slender delta wing.

The schematics of the delta wing and coordinate system to be used in the dynamic simulations are shown in figure 2. It is assumed that the wing has zero thickness and is mounted on a pivot.

Two coordinate systems are used: one inertial ground fixed frame of reference and one moving frame attached to the wing. All measurement and operations made with respect to the inertial frame are denoted with capital letters while lower case letters are used for the moving frame. The numerical problem is posed in the body fixed coordinate system. Therefore the relationship between variables in these two frames must be examined.

$$\begin{aligned}\Phi(\bar{R}, t) &= \Phi(\bar{r}, t) & p(\bar{R}, t) &= p(\bar{r}, t) \\ \nabla_R &= \nabla_r & \nabla_R^2 &= \nabla_r^2 \\ \left. \frac{d}{dt} \right|_r &= \left. \frac{d}{dt} \right|_R - (\bar{\Omega} \times \bar{r}) \cdot \nabla_r\end{aligned}$$

In the inertial frame of reference, the X axis is aligned with the freestream velocity. Before the dynamic simulation the wing is moved to its initial position by the following sequence:

- (a) a yaw-like rotation around the original Z axis through the angle β followed by
- (b) a pitch like rotation around the new position of Y axis through the angle α followed by
- (c) a roll like rotation around the final position of the X axis through the angle γ .

Once the initial position of the wing is fixed the dynamic simulation uses Euler angles ζ , η and ϕ to provide the wing motion.

The base vectors in the inertial frame and the freestream velocity are related to the body fixed frame as follows:

$$\begin{bmatrix} \bar{i} \\ \bar{j} \\ \bar{k} \end{bmatrix} = [C]_2 [C]_1 \begin{bmatrix} \bar{I} \\ \bar{J} \\ \bar{K} \end{bmatrix} \quad \begin{bmatrix} u \\ v \\ w \end{bmatrix}_b = [C]_2 [C]_1 \begin{bmatrix} V_\infty \\ 0 \\ 0 \end{bmatrix}$$

where

$$[C]_1 = \begin{bmatrix} \cos \alpha \cos \beta & \cos \alpha \sin \beta & -\sin \alpha \\ \sin \gamma \sin \alpha \cos \beta - \cos \gamma \sin \beta & \sin \gamma \sin \alpha \sin \beta + \cos \gamma \cos \beta & \sin \gamma \cos \alpha \\ \cos \gamma \sin \alpha \cos \beta + \sin \gamma \sin \beta & \cos \gamma \sin \alpha \sin \beta - \sin \gamma \cos \beta & \cos \gamma \cos \alpha \end{bmatrix}$$

$$[C]_2 = \begin{bmatrix} \cos \eta \cos \zeta & \cos \eta \sin \zeta & -\sin \eta \\ \sin \phi \sin \eta \cos \zeta - \cos \phi \sin \zeta & \sin \phi \sin \eta \sin \zeta + \cos \phi \cos \zeta & \sin \phi \cos \eta \\ \cos \phi \sin \eta \cos \zeta + \sin \phi \sin \zeta & \cos \phi \sin \eta \sin \zeta - \sin \phi \cos \zeta & \cos \phi \cos \eta \end{bmatrix}$$

Complex Potential

The Prandtl-Glauert equation

$$(1 - M_\infty^2) \frac{\partial^2 \Phi}{\partial x^2} + \frac{\partial^2 \Phi}{\partial y^2} + \frac{\partial^2 \Phi}{\partial z^2} = 0$$

is valid for supersonic and well as subsonic Mach numbers. If the wing is slender and the crossflow effect is dominant, the x derivative must be smaller than the other terms and the Laplace equation for the crossflow is obtained.

$$\frac{\partial^2 \Phi}{\partial y^2} + \frac{\partial^2 \Phi}{\partial z^2} = 0$$

Unlike the original Brown and Michael model, due to the asymmetry of the flow field, the delta wing cross plane will be transformed by conformal mapping to a circle plane and the circle theorem, which allows one immediately to write the complex potential in terms of the vortex system and its image will be used. The advantage of this approach is that the boundary conditions on the wing surface are satisfied exactly and the time dependency can be introduced through the boundary conditions.

The conformal mapping function is given as

$$\sigma = \xi + \frac{a^2}{\xi^2}$$

$$\xi = \frac{1}{2} \left(\sigma + \sqrt{\sigma^2 - 4a^2} \right)$$

where ξ represents the circle plane while σ represents the physical plane. Figure 3. is a sketch of the approximated flowfield in the crossflow physical plane and the circle plane. For a conical flow, the vortex strength increases linearly in the chordwise direction and therefore a feeding sheet is necessary in the model. This sheet is represented by a mathematical branch cut so that the potential function is single valued and is represented by the dotted line in figure 3. The cross flow velocities v_b and w_b are functions of the angle of attack, sideslip and roll angles and are defined previously. The steady flow field in the circle plane is represented by the superposition of a doublet with flow coming from two directions and two vortices. To satisfy the tangency condition, image vortices of the

opposite strength placed at $a^2/\bar{\xi}_v$, must be used. Using these elements, the steady complex potential can be written as

$$F_{steady} = \Phi + i\Psi = -iw_b \left(\xi - \frac{a^2}{\xi} \right) + v_b \left(\xi + \frac{a^2}{\xi} \right) + i \frac{\Gamma_l}{2\pi} \ln(\xi - \xi_l) - i \frac{\Gamma_l}{2\pi} \ln \left(\xi - \frac{a^2}{\xi_l} \right) \\ - i \frac{\Gamma_r}{2\pi} \ln(\xi - \xi_r) + i \frac{\Gamma_r}{2\pi} \ln \left(\xi - \frac{a^2}{\xi_r} \right)$$

The expression for the velocity at any point can be obtained by differentiating the previous equation with ξ .

$$W_{steady}(\xi) = \frac{dF}{d\xi} = v - iw = -iw_b \left(1 + \frac{a^2}{\xi^2} \right) + v_b \left(1 - \frac{a^2}{\xi^2} \right) + i \frac{\Gamma_l}{2\pi} \frac{1}{\xi - \xi_l} - i \frac{\Gamma_l}{2\pi} \frac{1}{\xi - \frac{a^2}{\xi_l}} \\ - i \frac{\Gamma_r}{2\pi} \frac{1}{\xi - \xi_r} + i \frac{\Gamma_r}{2\pi} \frac{1}{\xi - \frac{a^2}{\xi_r}}$$

In order to allow for unsteady motion of the wing the complex potential and the boundary conditions must be modified. The governing equation is the same for the unsteady case. However, since the Laplace equation does not explicitly depend on time, the boundary conditions must be time dependent and should be solved at each time step. The tangency condition for the unsteady case should be modified to state that the local fluid velocity normal to the wing should be equal to the local velocity of the wing itself. To satisfy this condition in the unsteady case, a potential function must be superimposed with the steady case to account for the unsteady boundary conditions. The derivation for this unsteady velocity potential is similar to that of Bisplinghoff, Ashley and Halfman^[3] for the unsteady flow on a pitching airfoil. The unsteady condition due to roll of the wing can be satisfied by using a source-sink sheet on the circle and the unsteady condition due to yaw can be satisfied using a doublet and freestream. The complex potential for a source-sink sheet around the circle and the doublet with freestream from the yaw can be expressed as

$$F_{unsteady} = \frac{1}{2\pi} \int_0^{2\pi} H^+ \ln(\xi - ae^{i\theta}) ad\theta - (x - \lambda Cr) \Omega_z \left(\xi + \frac{a^2}{\xi} \right)$$

The unsteady flow field can be obtained by differentiating the expression with respect to ξ .

$$W_{unsteady} = \frac{1}{2\pi} \int_0^{2\pi} \frac{H^+ a}{\zeta - ae^{i\theta}} d\theta - (x - \lambda Cr) \Omega_z \left(1 - \frac{a^2}{\xi^2}\right)$$

The unknown source-sink strength per unit length H^+ is given in terms of the local velocity of the wing as $H^+ = 2V_w$. The expressions will be transformed to the circle plane where

$$V_w|_{physical} = y \Omega_x = 2a \Omega_x \cos \theta$$

$$V_w|_{circle} = 2y \Omega_x \sin \theta = 4a \Omega_x \sin \theta \cos \theta$$

The expression for the unsteady complex velocity in the circle plane can be written as

$$W_{unsteady} = \frac{4a^2 \Omega_x}{\pi} \int_0^{2\pi} \frac{\sin \theta \cos \theta}{\zeta - ae^{i\theta}} d\theta - (x - \lambda Cr) \Omega_z \left(1 - \frac{a^2}{\xi^2}\right)$$

Therefore, the total complex velocity in the circle plane can be written as

$$W(\xi) = v - iw = -iw_b \left(1 + \frac{a^2}{\xi^2}\right) + v_b \left(1 - \frac{a^2}{\xi^2}\right) + i \frac{\Gamma_l}{2\pi} \frac{1}{\xi - \xi_l} - i \frac{\Gamma_l}{2\pi} \frac{1}{\xi - \frac{a^2}{\xi_l}} - i \frac{\Gamma_r}{2\pi} \frac{1}{\xi - \xi_r} + i \frac{\Gamma_r}{2\pi} \frac{1}{\xi - \frac{a^2}{\xi_r}} + \frac{4a^2 \Omega_x}{\pi} \int_0^{2\pi} \frac{\sin \theta \cos \theta}{\xi - ae^{i\theta}} d\theta - (x - \lambda Cr) \Omega_z \left(1 - \frac{a^2}{\xi^2}\right)$$

To obtain the pressure distribution on the wing, the tangential velocity due to the unsteady motion must be known. However, the equation for the unsteady velocities is singular on the wing surface and cannot be used. Therefore, the expression for the tangential velocity on the circle plane due to the roll and yaw given by Bisplinghoff et. al.[3] will be used

$$V_t = \frac{2}{\pi} \int_0^\pi \frac{V_w \sin^2 \vartheta}{\cos \vartheta - \cos \theta} d\vartheta + 2(x - \lambda Cr) \Omega_z \sin \theta$$

By substituting the expression for the wing velocity in the physical plane, the tangential velocity can be found.

$$V_t = \frac{4\Omega_x a}{\pi} \int_0^\pi \frac{\cos \vartheta \sin^2 \vartheta}{\cos \vartheta - \cos \theta} d\vartheta + 2(x - \lambda Cr) \Omega_z \sin \theta = \frac{\Omega_x a}{\pi} \int_0^\pi \frac{\cos \vartheta - \cos^3 \vartheta}{\cos \vartheta - \cos \theta} d\vartheta + 2(x - \lambda Cr) \Omega_z \sin \theta = -2\Omega_x a (1 - 2\sin^2 \theta) + 2(x - \lambda Cr) \Omega_z \sin \theta$$

Kutta Condition

Normally, the separation point for a slender sharp edged delta wing is fixed at the leading edge. However, to study the effects of displaced separation, it is assumed that the separation point is located at an arbitrary point σ_s . This requirement of a separation point at σ_s is expressed in the present formulation as

$$W(\sigma_s) = W(\xi_s) \frac{d\xi}{d\sigma} \Big|_{\sigma_s} = W(\xi_s) \frac{\xi^2}{\xi^2 - a^2} \Big|_{\sigma_s} = 0$$

Therefore, for the left and right separation points we obtain the following two conditions.

$$\begin{aligned} -iw_b \left(1 + \frac{a^2}{\xi_s^2} \right) + v_b \left(1 - \frac{a^2}{\xi_s^2} \right) + i \frac{\Gamma_l}{2\pi} \frac{1}{\xi_s - \xi_l} - i \frac{\Gamma_l}{2\pi} \frac{1}{\xi_s - \frac{a^2}{\xi_l}} - i \frac{\Gamma_r}{2\pi} \frac{1}{\xi_s - \xi_r} \\ + i \frac{\Gamma_r}{2\pi} \frac{1}{\xi_s - \frac{a^2}{\xi_r}} + \frac{4a^2 \Omega_x}{\pi} \int_0^{2\pi} \frac{\sin \theta \cos \theta}{\xi_s - ae^{i\theta}} d\theta - (x - \lambda Cr) \Omega_x \left(1 - \frac{a^2}{\xi_s^2} \right) = 0 \end{aligned}$$

Note that the integral is singular but has a finite value at $\xi_s = ae^{i\theta}$. Hence to avoid any numerical problems an adaptive integration scheme is used.

Force Free Condition

In an actual fluid, the fluid pressure is continuous everywhere. However, for the present model the feeding sheet is modeled by a branch cut which gives a jump in the potential function which in turn creates a pressure discontinuity. The force-free condition is based on the fact that there can be no unbalanced forces in the fluid, hence the pressure forces from the feeding sheet must be balanced by the force on the vortices.

The pressure jump across the feeding sheet in terms of the pressure coefficient can be shown to be

$$\Delta C_p = \frac{2}{V_\infty^2} \left(u_b \frac{d\Gamma}{dx} + \dot{\Gamma} \right)$$

The force exerted by the feeding sheet can be obtained by integrating ΔC_p from the separation point to the vortex and multiplying by the dynamic pressure.

$$F_{left \ feeding \ sheet} = -i\rho \left(u_b \frac{d\Gamma_l}{dx} + \dot{\Gamma}_l \right) (\sigma_l - \sigma_s) \quad F_{right \ feeding \ sheet} = i\rho \left(u_b \frac{d\Gamma_r}{dx} + \dot{\Gamma}_r \right) (\sigma_r - \sigma_s)$$

The force exerted on the vortex itself is given by the Kutta-Joukowski theorem

$$F_{\text{left vortex}} = i\rho\Gamma_l \left[\overline{W(\sigma_l)} - u_b \frac{d\sigma_l}{dx} - \frac{d\sigma_l}{dt} \Big|_R \right] \quad F_{\text{right vortex}} = -i\rho\Gamma_r \left[\overline{W(\sigma_r)} - u_b \frac{d\sigma_r}{dx} - \frac{d\sigma_r}{dt} \Big|_R \right]$$

where $\frac{d\sigma_v}{dt} \Big|_R$ is the velocity of the vortex with respect to the inertial frame and $u_b \frac{d\sigma_v}{dx}$ is due to the inclination of the line vortices with respect to the freestream velocity.

From the force free conditions, the force from the feeding sheet must cancel the force from the vortex. Combining the equations for both the left and right vortex we have

$$\frac{d\sigma_v}{dt} \Big|_R = -u_b \frac{d\sigma_v}{dx} + \overline{W(\sigma_v)} - \left(u_b \frac{d\Gamma_v}{dx} + \frac{d\Gamma_v}{dt} \right) \frac{\sigma_v - \sigma_s}{\Gamma_v}$$

To simplify the equations, the conical flow assumption will be used. For conical flow the vortex strength and position are linearly increasing functions of x . Therefore,

$$\frac{d\sigma_v}{dx} = \frac{\sigma_v}{2a} \tan \epsilon \quad \frac{d\Gamma_v}{dx} = \frac{\Gamma_v}{2a} \tan \epsilon$$

All the equations up to this point have been defined with respect to the ground fixed inertial frame. Since the wing will go into motion, it is convenient to transform the equations to the body fixed frame. We have previously shown that for the two ground fixed and body fixed coordinate systems

$$\frac{d\sigma_v}{dt} \Big|_R = \frac{d\sigma_v}{dt} \Big|_r + \Omega \times r$$

All equations will be solved in the circle plane and can be transformed by

$$\sigma = \xi + \frac{a^2}{\xi^2} \quad \frac{d\sigma_v}{dt} \Big|_r = \frac{d\sigma_v}{d\xi_v} \frac{d\xi_v}{dt} \Big|_r = \frac{\xi_v^2 - a^2}{\xi_v^2} \frac{d\xi_v}{dt} \Big|_r$$

Milne-Thompson^[11] has shown that one must be careful when transforming equation carrying vortex expressions to different planes, because the solution will not be the same when transformed back to the physical plane. Therefore to calculate the velocity at the vortex center, the following term must be added.

$$\overline{W(\sigma_v)} = \overline{W(\xi_v)} \frac{\xi_v^2}{\xi_v^2 - a^2} - i \frac{\Gamma}{2\pi} \frac{1}{2} \frac{d}{d\xi} \left(\frac{d\xi}{d\sigma} \right) \Big|_v = \overline{W(\xi_v)} \frac{\xi_v^2}{\xi_v^2 - a^2} \pm i \frac{\Gamma}{2\pi} \frac{\xi_v a^2}{(\xi_v^2 - a^2)^2}$$

The final form of the force free condition can be written as

$$\frac{d\xi_v}{dt} \Big|_r = \frac{\xi_v^2}{\xi_v^2 - a^2} \left\{ \overline{W(\xi_v)} \frac{\xi_v^2}{\xi_v^2 - a^2} \pm \frac{\Gamma}{2\pi} \frac{\xi_v a^2}{(\xi_v^2 - a^2)^2} - \frac{u_b \tan \epsilon}{2a} \left[2 \left(\xi_v + \frac{a^2}{\xi_v} \right) - \left(\xi_s + \frac{a^2}{\xi_s} \right) \right] \right\}$$

$$-i \frac{\Gamma_v}{\Gamma_v} \left[\left(\xi_v + \frac{a^2}{\xi_v} \right) - \left(\xi_s + \frac{a^2}{\xi_s} \right) \right] - i \Omega_x \frac{\xi_v (\xi_v^2 + a^2)}{(\xi_v^2 - a^2)} - (x - \lambda Cr) \Omega_z$$

The final step is to transform the equations into conical variables to eliminate the chordwise dependence of the steady terms. The vortex position, strength and time will be non-dimensionalized by the following variables.

$$\xi^* = \frac{\xi}{a} \quad \kappa = \frac{\Gamma}{2\pi a V_\infty} \quad t^* = \frac{t V_\infty}{Cr}$$

The final system of equations is

$$-i \frac{w_b}{V_\infty} \left(1 + \frac{1}{\xi_s^{*2}} \right) + \frac{v_b}{V_\infty} \left(1 - \frac{1}{\xi_s^{*2}} \right) + i \left(\frac{\kappa_l}{\xi_s^* - \xi_l^*} - \frac{\kappa_l}{\xi_s^* - \frac{1}{\xi_l^*}} - \frac{\kappa_r}{\xi_s^* - \xi_r^*} + \frac{\kappa_r}{\xi_s^* - \frac{1}{\xi_r^*}} \right) + \frac{2x \tan \epsilon \Omega_x^*}{\pi Cr} \int_0^{2\pi} \frac{\sin \theta \cos \theta}{\xi_s^* - e^{i\theta}} d\theta - \left(\frac{x}{Cr} - \lambda \right) \Omega_z^* \left(1 - \frac{1}{\xi_s^{*2}} \right) = 0$$

$$\frac{d\xi_v^*}{dt} \Big|_r = \frac{\xi_v^{*2}}{\xi_v^{*2} - 1} \left\{ \left[\frac{W_v(\xi_v^*)}{\xi_v^{*2} - 1} \pm i \frac{\xi_v^* \kappa_v}{(\xi_v^{*2} - 1)^2} \right] \frac{2Cr}{x \tan \epsilon} - \frac{u_b}{V_\infty} \frac{Cr}{x} \left[2 \left(\xi_v^* + \frac{1}{\xi_v^*} \right) - \left(\xi_s^* + \frac{1}{\xi_s^*} \right) \right] - \frac{\kappa_v}{\kappa_v} \left[\left(\xi_v^* + \frac{1}{\xi_v^*} \right) - \left(\xi_s^* + \frac{1}{\xi_s^*} \right) \right] \right\} - i \Omega_x^* \frac{\xi_v^* (\xi_v^{*2} + 1)}{(\xi_v^{*2} - 1)} - \frac{2}{\tan \epsilon} \left(1 - \frac{\lambda Cr}{x} \right) \Omega_z^*$$

where

$$W_v(\xi_v^*) = -i \frac{w_b}{V_\infty} \left(1 + \frac{1}{\xi_s^{*2}} \right) + \frac{v_b}{V_\infty} \left(1 - \frac{1}{\xi_s^{*2}} \right) + i \left(\frac{\kappa_l}{\xi_s^* - \xi_l^*} - \frac{\kappa_l}{\xi_s^* - \frac{1}{\xi_l^*}} - \frac{\kappa_r}{\xi_s^* - \xi_r^*} + \frac{\kappa_r}{\xi_s^* - \frac{1}{\xi_r^*}} \right) + \frac{2x \tan \epsilon \Omega_x^*}{\pi Cr} \int_0^{2\pi} \frac{\sin \theta \cos \theta}{\xi_s^* - e^{i\theta}} d\theta - \left(\frac{x}{Cr} - \lambda \right) \Omega_z^* \left(1 - \frac{1}{\xi_s^{*2}} \right)$$

We now have six unknowns (two normal and spanwise vortex positions and two vortex strengths) and six equations (two from the Kutta condition and four from the zero force condition).

Equations of Motion

For a thin delta wing mounted on a ball and socket sting at point c, as shown in figure 2, the Euler rigid body rotational equations of motion are of the form

$$\overline{M}_c = I_c \ddot{\overline{\Omega}} + \overline{\Omega} \times (I_c \cdot \overline{\Omega})$$

where \overline{M}_c is the external moments around point c, $\overline{\Omega}$ is the wing angular velocity vector and I_c is the inertia matrix about c. For the special case of principal axes,

$$I_c = \begin{bmatrix} I_{xx} & 0 & 0 \\ 0 & I_{yy} & 0 \\ 0 & 0 & I_{zz} \end{bmatrix}$$

where

$$I_{xx} = \frac{1}{6} \rho_w Cr^4 \tan^3 \varepsilon \quad I_{yy} = \rho_w Cr^4 \tan \varepsilon \left[\frac{1}{18} + \left(\lambda - \frac{2}{3} \right)^2 \right]$$

$$I_{zz} = I_{xx} + I_{yy} = \left[\frac{\tan^2 \varepsilon}{6} + \frac{1}{18} + \left(\lambda - \frac{2}{3} \right)^2 \right] \rho_w Cr^4 \tan \varepsilon$$

The equation of motion can be written in component form

$$M_x = I_{xx} \dot{\Omega}_x + (I_{zz} - I_{yy}) \Omega_z \Omega_y$$

$$M_y = I_{yy} \dot{\Omega}_y + (I_{xx} - I_{zz}) \Omega_x \Omega_z$$

$$M_z = I_{zz} \dot{\Omega}_z + (I_{yy} - I_{xx}) \Omega_y \Omega_x$$

The components of $\overline{\Omega}$ can be written in terms of Euler angles using the following relations.

$$\begin{bmatrix} \Omega_x \\ \Omega_y \\ \Omega_z \end{bmatrix} = \begin{bmatrix} -\sin \eta & 0 & 1 \\ \sin \phi \cos \eta & \cos \phi & 0 \\ \cos \phi \cos \eta & -\sin \phi & 0 \end{bmatrix} \begin{bmatrix} \dot{\zeta} \\ \dot{\eta} \\ \dot{\phi} \end{bmatrix}$$

Differentiating these equations and noting that $I_{zz} = I_{yy} + I_{xx}$, the equations of motion can be rewritten as

$$M_x = I_{xx} (\ddot{\phi} - \sin \eta \dot{\zeta}) + I_{xx} [\cos \phi \sin \phi (\cos^2 \eta \dot{\zeta}^2 - \dot{\eta}^2) - 2 \cos \eta \sin^2 \phi \dot{\eta} \dot{\zeta}]$$

$$M_y = I_{yy} (\cos \phi \ddot{\eta} + \sin \phi \cos \eta \dot{\zeta}) + I_{yy} [\sin \eta (\cos \eta \cos \phi \dot{\zeta}^2 - 2 \sin \phi \dot{\eta} \dot{\zeta})]$$

$$M_z = I_{zz} (\cos \phi \cos \eta \ddot{\zeta} - \sin \phi \ddot{\eta}) + I_{xx} (\sin \eta \cos \eta \sin \phi \dot{\zeta}^2 - 2 \sin \phi \cos \eta \dot{\phi} \dot{\zeta} - 2 \cos \phi \dot{\phi} \dot{\eta}) \\ - I_{yy} (\sin \eta \cos \eta \sin \phi \dot{\zeta}^2 + 2 \cos \phi \sin \eta \dot{\eta} \dot{\zeta})$$

The external moment terms are generated by gravity, frictional damping and the aerodynamic forces.

$$\text{gravity terms: } \rho_w Cr^3 \tan \epsilon \left(\frac{2}{3} - \lambda \right) g (\cos \phi \cos \eta \bar{j} - \sin \phi \cos \eta \bar{k})$$

$$\text{damping terms: } -\mu_x (\dot{\phi} - \sin \eta \dot{\zeta}) \bar{i} - \mu_y (\cos \phi \dot{\eta} + \sin \phi \cos \eta \dot{\zeta}) \bar{j} - \mu_z (\cos \phi \cos \eta \dot{\zeta} - \sin \phi \dot{\eta}) \bar{k}$$

$$\text{aerodynamic moment terms: } \frac{1}{2} \rho V_\infty^2 Cr^3 \tan \epsilon (C_x \bar{i} + C_y \bar{j} + C_z \bar{k})$$

where

$$C_x = \frac{\tan \epsilon}{3} \int_0^{2\pi} (C_{p_1} - C_{p_2}) \sin \theta \cos \theta d\theta \quad C_y = \left(\frac{\lambda}{2} - \frac{1}{3} \right) \int_0^{2\pi} (C_{p_1} - C_{p_2}) \sin \theta d\theta \quad C_z = 0$$

The pressure coefficient is obtained using the unsteady Bernoulli equation.

$$C_p = 1 - \left(\frac{u_b}{V_\infty} \right)^2 - \frac{2u_b \Phi_x}{V_\infty^2} - \frac{\Phi_x^2 + \Phi_y^2 + \Phi_z^2}{V_\infty^2} - \frac{2 \frac{\partial \Phi}{\partial t} \Big|_R}{V_\infty^2}$$

To transform the C_p expression to the body fixed frame, we have previously shown that

$$\frac{\partial \Phi}{\partial t} \Big|_R = \frac{\partial \Phi}{\partial t} \Big|_r + (\bar{\Omega} \times \bar{r}) \cdot \nabla_r \Phi$$

All the dynamic simulation results which will be shown later do not contain the frictional damping term. Nonetheless, these terms can be added to simulate the friction from the bearings which is present in the actual experiments.

The equations of motion can be rewritten in matrix form

$$\begin{bmatrix} \ddot{\phi} \\ \ddot{\eta} \\ \ddot{\zeta} \end{bmatrix} = \begin{bmatrix} 1 & \sin \phi \tan \eta & \cos \phi \tan \eta \\ 0 & \cos \phi & -\sin \phi \\ 0 & \sin \phi / \cos \eta & \cos \phi / \cos \eta \end{bmatrix} \begin{bmatrix} R_x \\ R_y \\ R_z \end{bmatrix}$$

where

$$R_x = \frac{1}{2} \rho V_\infty^2 Cr^3 \frac{\tan \epsilon}{I_{xx}} C_x - \frac{\mu_x}{I_{xx}} (\dot{\phi} - \sin \eta \dot{\zeta}) - \cos \phi \sin \phi (\cos^2 \eta \dot{\zeta}^2 - \dot{\eta}^2) + 2 \cos \eta \sin^2 \phi \dot{\eta} \dot{\zeta}$$

$$R_y = \frac{1}{2} \rho V_\infty^2 Cr^3 \frac{\tan \epsilon}{I_{yy}} C_y - \frac{\mu_y}{I_{yy}} (\cos \phi \dot{\eta} + \sin \phi \cos \eta \dot{\zeta}) + \frac{\rho_w}{I_{yy}} Cr^3 \tan \epsilon \left(\frac{2}{3} - \lambda \right) g \cos \phi \cos \eta \\ - \sin \eta (\cos \eta \cos \phi \dot{\zeta}^2 - 2 \sin \phi \dot{\eta} \dot{\zeta})$$

$$R_z = \frac{1}{2} \rho V_\infty^2 C r^3 \frac{\tan \varepsilon}{I_x} C_z - \frac{\mu_z}{I_x} (\cos \phi \cos \eta \dot{\zeta} - \sin \phi \dot{\eta}) - \frac{\rho_w}{I_x} C r^3 \tan \varepsilon \left(\frac{2}{3} - \lambda \right) g \sin \phi \cos \eta$$

$$+ 2 \frac{I_{xz}}{I_x} (\sin \phi \cos \eta \dot{\phi} \dot{\zeta} + \cos \phi \dot{\phi} \dot{\eta}) + \frac{I_{yy} - I_{xx}}{I_x} \sin \eta \cos \eta \sin \phi \dot{\zeta}^2 + 2 \frac{I_{yy}}{I_x} \cos \phi \sin \eta \dot{\eta} \dot{\zeta}$$

For the two degree of freedom case, $\ddot{\zeta} = \dot{\zeta} = \zeta = 0$. After some manipulation of the equations and changing into non-dimensional form for roll and yaw we obtain

$$\ddot{\phi}^* = \frac{1}{2} \rho C r^5 \frac{\tan \varepsilon}{I_x} C_x - \frac{C r \mu_x}{V_\infty I_x} \dot{\phi}^* - \cos \phi \sin \phi \dot{\zeta}^{*2}$$

$$\dot{\zeta}^* = \frac{-\mu_z C r}{I_x V_\infty} \dot{\zeta}^* - \frac{\rho_w C r^5}{I_x V_\infty^2} \tan \varepsilon \left(\frac{2}{3} - \lambda \right) g \tan \phi + 2 \frac{I_{xz}}{I_x} \tan \phi \dot{\phi}^* \dot{\zeta}^*$$

For the one degree of freedom case there is an additional constraint, $\ddot{\zeta} = \dot{\zeta} = \zeta = 0$. In non-dimensional form, the equation of motion for roll is given as

$$\ddot{\phi}^* = \frac{1}{2} \rho C r^5 \frac{\tan \varepsilon}{I_x} C_x - \frac{C r \mu_x}{V_\infty I_x} \dot{\phi}^*$$

To begin the dynamic simulation, the wing is first set at an initial position. The static flow field is then solved and the wing is released. The pressure distribution is calculated and the aerodynamic moments are obtained by integrating the pressure distributions. The new wing position and angular velocities are found from solving the equations of motion. Because the method can only predict unit time steps, a predictor-corrector method by Carnahan^[5] is used for time marching instead of a Runge-Kutta method. Using the new wing position and velocity, the unsteady vortex position and strength are obtained using the Kutta and zero-force conditions. A flow chart of the described process can be seen in figure 4.

Results and Discussion

For analyzing wing rock aerodynamics, an extremely useful tool is the concept of energy exchange proposed by Nguyen et. al^[14]. During wing rock motion, the energy added or extracted from the system for a certain time interval can be expressed as

$$\Delta E = \frac{1}{2} \rho V_{\infty}^2 Cr \int_{t_1}^{t_2} C_l(t) \dot{\phi}(t) dt = \frac{1}{2} \rho V_{\infty}^2 Cr \int_{\phi_1}^{\phi_2} C_l(\phi) d\phi.$$

Therefore, for a steady state wing rock limit cycle the net energy exchange is given by

$$\Delta E = \frac{1}{2} \rho V_{\infty}^2 Cr \oint C_l(\phi) d\phi.$$

From figure 5 it can be seen that for a counterclockwise loop, energy is added to the system therefore the motion is destabilized while for a clockwise loop, energy is extracted from the system and the motion is stabilized. The amount of the net energy exchange, ΔE is proportional to the area contained in the loop.

One Degree of Freedom Wing Rock

Figure 6 shows the time history of one degree of freedom wing rock where there is no sideslip and separation point displacement. The angle of attack is 20° and the semi-apex angle of the delta wing is 10° . The wing is released at two different initial angles, 0.5° and 85° . The wing rock amplitude and frequency is the same for both cases assuring that the motion is independent of the initial conditions and is a true limit cycle.

The steady state total sectional roll moment coefficient plots are shown in figure 7(a). Using the energy exchange concept, it is shown that the clockwise destabilizing lobe occurs at small roll angles, while the two counterclockwise stabilizing lobes occur at large roll angles. The area of the destabilizing lobe is identical to the area of the two damping lobes indicating there is no energy exchange and hence steady state is observed. By showing the sectional roll moment coefficients for the top and bottom surfaces separately in figure 7(b), we can see that all the instability comes from the top surface while the bottom surfaces only contributes to the damping.

The roll moment coefficients plots have shown when and where the damping and destabilizing occur but do not tell us the aerodynamic mechanism for this phenomena. The physics underlying the motion can be explained by figure 8, the dynamic vortex position and strength. Figures 8(a) & (b) show the static and dynamic, spanwise and normal position of the vortex. The spanwise vortex position does not vary much from the static position during wing rock and leads or lags depending on the roll angle. However, the vortex position normal to the wing surface always lags the static position by a large

amount, regardless of the roll angle. This vortex position lag gives the destabilizing moments which initiate the wing rock motion. The hysteresis is largest at small roll angles and this coincides with the roll angles where the destabilizing lobes appear in figure 7(a). If there were no damping the wing rock motion would continue to grow without bound and therefore damping is necessary to generate limit cycle motion. The damping lobes can be explained from the static and dynamic vortex strength shown in figure 8(c). The dynamic vortex strength is constantly leading the static vortex strength. This leading is largest at large roll angles and this also coincides with the damping lobe positions shown in figure 7(a). Steady state oscillation occurs when the instability from the vortex normal position lag balances the damping from the vortex strength lead. With the mechanisms of wing rock identified, the model was used to investigate the effects of various parameters on the aerodynamics of wing rock.

Effect of Angle of Attack

It is well known that wing rock does not occur at low angles of attack and as the angle of attack is increased an aircraft is more susceptible to wing rock motion. Therefore, the effect of angle of attack on the wing rock motion was studied.

Figure 9 shows that by keeping the wing semi-apex angle the same as in the previous case but by lowering the angle of attack to 10° , the wing rock motion will damp and no limit cycle will be observed. Figure 10(a) shows the total sectional roll moment coefficient for one cycle. The counterclockwise loop direction shows that the whole cycle is damped and figure 10(b) shows that both the top and bottom wing surfaces contribute to the damping. No instability lobes are present. However, if the angle of attack is raised to 30° with the same wing configuration, figure 11 shows that the wing motion will diverge. Again by examining the total sectional roll moment coefficient diagram, figure 12(a), the loop is in the clockwise direction, indicating an energy addition to the system and hence destabilization. Figure 12(b) shows that the bottom surface adds damping to the motion. However, the top surface instability lobe is so large that it overwhelms the bottom surface and gives oscillatory divergence. In actual flight, oscillatory divergence will not occur because as the wing rock motion grows vortex bursting will occur. The vortex bursting contributes to a sudden loss of lift of the wing and consequently has a stabilizing effect on wing rock. The present model does not predict vortex breakdown and therefore oscillatory divergence behavior is exhibited.

The aerodynamic model shows the effect of angle of attack by qualitatively explaining why wing rock does not appear at certain low incidence angles and why wing rock is more susceptible at higher angles of attack.

Effect of Yaw Angle

To see the effect of yaw on the one degree of freedom wing rock, it is assumed that the wing is placed at a certain fixed yaw angle and left free to roll. Even though the wing is symmetric, figures 13(a) and (b) show asymmetric amplitudes of wing rock due to the 5° sideslip angle of the wing. Again, it can be seen that even for the case with sideslip the wing rock amplitude and frequency is independent of the initial roll angle.

Figure 14(a) shows the total sectional roll moment coefficient during one steady wing rock cycle at 5° yaw angle. It is interesting to note that the shape of the curve is almost identical to that of figure 7(a), the wing rock case with no yaw. The only difference is that the curve in figure 14(a) is shifted to the right by 14°. Again, figure 14(b) gives an identical plot to that of figure 7(b) and the only difference is the shift to the right. All other trends, like the damping and instability lobe sizes or top and bottom wing surface contributions to the wing rock motion are yaw independent. It has been shown that the wing rock motion is strongly dependent on the angle of attack, yaw angle and semi-apex angle of the wing. Therefore, this shifting to the right can be explained by the concept of effective angle of attack, effective sideslip and effective semi-apex angle.

An effective angle is defined as the angle that the wing "feels". For example, even if the angle of attack is fixed, as the wing rolls, the angle of attack that the wing feels, i.e. the effective angle of attack will reduce as the roll angle increases and will reach 0° as the roll angle goes to 90° when there is no yaw.

From simple trigonometry, the effective angle expressions are given as

$$\alpha_{eff} = \tan^{-1}\left(\frac{w_b}{u_b}\right) = \tan^{-1}\left[\frac{\sin \alpha \cos \beta \cos(\gamma + \phi) + \sin \beta \sin(\gamma + \phi)}{\cos \alpha \cos \beta}\right]$$

$$\beta_{eff} = \tan^{-1}\left(\frac{-v_b}{u_b}\right)$$

$$= \tan^{-1}\left[\frac{\sin \alpha \cos \beta (\cos \gamma \sin \phi - \sin \gamma \cos \phi) + \sin \beta (\cos \gamma \cos \phi + \sin \gamma \sin \phi)}{\cos \alpha \cos \beta}\right]$$

$$\epsilon_{eff, left} = \epsilon - \beta_{eff} \quad \epsilon_{eff, right} = \epsilon + \beta_{eff}$$

Figure 15 shows these effective angles for both 0° and 5° sideslip. It can be seen from the figure that the effect of the sideslip is to shift the effective angles which determine the vortex position and strength. Hence the wing rock motion shifts to the right as the angle of sideslip goes from 0° to 5°. The effective angles are also shifted about 14°, which is the same amount that the sectional roll moment diagrams were displaced.

If we compare the wing rock amplitude for the zero side slip case (figure 6) and the 5° sideslip case (figure 13), again we can see that for the positive roll angles the wing rock amplitude is increased by an amount of 14° while for the negative roll angles the amplitude is decreased by 14°. The dynamic spanwise and normal vortex positions and unsteady vortex strength diagrams are shown in figure 16. These show the same shape and magnitude as for the zero sideslip case, but are once again shifted to the right by 14°. Therefore, the wing rock mechanism for wing rock with sideslip is the same as the zero sideslip case, but the effect of sideslip is to shift the roll angles by an amount which depends on the amount of the initial yaw angle of the wing.

Effect of Separation Point Displacement

It has been shown by Wong^[18] that one degree of freedom wing rock can be controlled by active means such as changing the leading edge vortex separation point by blowing. Although for thin delta wings the separation point is fixed at the leading edge, the model was generalized to be able to change the separation point locations and to observe the corresponding effect on the wing rock motion.

The Brown and Michael model shows that the general effect of moving the separation point inboard is to move the vortex inward and slightly downward and also to weaken the vortex strength. Figure 17 shows the wing rock time history for two initial conditions when the right separation point is displaced inboard by 1% of the semi-span. It can be seen that there is very little change in the negative roll angle wing rock amplitude compared to the no separation displacement case, figure 6, while the positive roll angle wing rock amplitude is reduced. The total sectional roll moment diagram, figure 18(a) shows that unlike the case of wing rock with sideslip, there is no roll angle shifting. The damping lobe areas are identical to the area of the instability lobe indicating there is no energy exchange. However, the enclosed areas of the two damping lobes are different, which explains why the wing rock amplitudes for positive and negative roll angles are different. Once again it can be seen from figure 18(b) that the bottom surface contributes only to the damping while all the instability comes from the top surface. For positive roll angles, the top surface shows a very small damping lobe while the damping lobe for the negative roll angles is quite large. Figure 19(b), the vortex normal position hysteresis which gives the instability at small angles is quite symmetric with respect to 0°. This corresponds to the nearly symmetric clockwise instability lobe in figure 18. The vortex strength hysteresis responsible for the damping has a small magnitude for positive roll angles and a large magnitude for negative roll angles which is again consistent with the results in figure 18. Therefore, the asymmetry of the wing rock amplitude for the

displacement separation case results mainly from the different size damping lobes caused by the asymmetric vortex strength hysteresis.

The fact that even a small separation point displacement (1% of the semi-span) can give a large difference in wing rock amplitude, suggests that moving the separation point by inboard spanwise blowing can be a powerful mechanism for controlling the wing rock motion.

Effect of Wing Inertia

To see the effect of wing inertia, the roll moment of inertia, I_{xx} of a wing of semi-apex angle 10° at an angle of attack of 20° was varied from $90 \text{ kg}\cdot\text{m}^2$ to $210 \text{ kg}\cdot\text{m}^2$ in $30 \text{ kg}\cdot\text{m}^2$ intervals.

Figure 20(a) shows that the wing rock amplitude is independent of the wing inertia. The wing rock frequency was also examined. Figure 20(b) shows that the inverse square root of the inertia was almost linearly proportional to the wing rock frequency. This indicates that the wing rock behaves like a second order linear oscillator. The same results for the inertia variation were seen in the experiments of Arena^[1] and once again shows that the model captures the qualitative trends seen in experiments.

Two Degree of Freedom Wing Rock

Experiments to understand and actively control the two degrees of freedom wing rock in roll and yaw are being conducted in the Stanford low speed wind tunnel by Pedreiro. However, before an efficient control algorithm to stabilize the motion can be devised, the aerodynamics of this phenomena must be fully understood. Also because of the various parameters involved in the experiments, a general aerodynamic model where various control laws can be tested before actual implementation in the wind tunnel is necessary. Therefore, the previous one degree of freedom model was extended to accommodate yaw motion in the wing plane as an additional degree of freedom.

Figures 21(a) and (b) show how the roll and yaw Euler angles and the effective angle of attack, effective sideslip and effective roll angle change with time. Unlike the one degree of freedom case, no limit cycle was observed. Various initial conditions and damping terms of different magnitudes were added to the equations of motion but still no limit cycle could be noticed. Figure 22 shows how the top and bottom wing surface sectional roll moment coefficients change as a function of roll and yaw angles. The energy exchange concept cannot be used, because no organized damping or instability lobes are formed. Figures 23 and 24 show how the unsteady spanwise and normal vortex positions and strength change with the Euler roll and yaw angles. Unlike the one degree of

freedom case, no analysis of the mechanism of the motion can be made by looking at the lead or lag of the vortex position or strength.

Conclusions

Following the work of Arena, an aerodynamic model using an extension of the Brown and Michael model has been developed to capture the dominant features of wing rock motion. For the one degree of freedom case, the model explains the mechanisms which generate and sustain wing rock. Instability which drives the wing rock motion comes from the lag in the vortex position normal to the wing surface which mainly occurs at small roll angles while the damping comes from the unsteady vortex strength lead. Steady state wing rock occurs when the instability from the vortex position lag, balances the damping from the vortex strength lead.

The effect of increasing the angle of attack is to enlarge the instability lobe and to make the wing more susceptible to wing rock. The effect of sideslip on the wing rock motion has been shown to give a shift in the roll angle and hence give an asymmetric wing rock amplitude. The reason behind this roll shifting has been explained by the effective angle concept. Moving the separation point also gives asymmetric wing rock amplitudes by changing the sizes of the damping lobes.

For the two degree of freedom case no limit cycle was observed. However, the two degree of freedom model can still be used to test various control algorithms.

Future work can include adding a pitching motion of the wing to create a three degree of freedom wing rock model.

References

- [1] Arena, Jr., A. S., "An Experimental and Computational Investigation of Slender Wings Undergoing Wing Rock", Ph.D. Thesis, Department of Aerospace and Mechanical Engineering, University of Notre Dame, 1992.
- [2] Arena, Jr., A. S. and Nelson, R. C. and Schiff, L. B., "An Experimental Study of the Nonlinear Dynamic Phenomenon Known as Wing Rock", AIAA 90-2812, August, 1990.
- [3] Bisplinghoff, R. L., Ashley, H. and Halfman, R. L., *Aeroelasticity*, Addison-Wesley Publishing Company Inc., Massachusetts, 1955.
- [4] Brown, C. E. and Michael, W. H., "On Slender Delta Wings with Leading Edge Separation", NACA TN 3430, Jan. 1955
- [5] Carnahan, B., Luther, H. A. and Wilkes, J. O., *Applied Numerical Methods*, John Wiley & Sons, Inc., New York, 1969.
- [6] Elzebda, J., "Two Degree of Freedom Subsonic Wing Rock and Nonlinear Aerodynamic Interference", Ph.D. Thesis, Department of Engineering Science and Mechanics, Virginia Polytechnic Institute and State University, 1986.
- [7] Ericsson, L. E., "The Fluid Mechanics of Slender Wing Rock", *Journal of Aircraft*, Vol. 21, May 1984.
- [8] Ericsson, L. E., "Various Sources of Wing Rock", *Journal of Aircraft*, Vol. 27, June 1990.
- [9] Greenwood, D. T., *Principles of Dynamics*, Prentice-Hall, New-Jersey, 1965.
- [10] Milne-Thompson, L. M., *Theoretical Aerodynamics*, Fourth Edition, Dover Publications Inc., New York, 1958.
- [11] Milne-Thompson, L. M., *Theoretical Hydrodynamics*, Fourth Edition, The Macmillan Company, New York, 1960.
- [12] Mourtos, N. J., "Control of Vortical Separation on Conical Bodies", Ph.D. Thesis, Department of Aeronautics and Astronautics, Stanford University, 1987.
- [13] Nayfeh, A., Elzebda, J. and Mook, D., "Analytical Study of the Subsonic Wing Rock Phenomenon for Slender Delta Wings", *Journal of Aircraft*, Vol. 26, September 1989.
- [14] Nguyen, L. T., Yip, L. P. and Cambers, J. R., "Self-Induced Wing Rock of Slender Delta Wings", AIAA 81-1883, 1981.

[15] Pedreiro, N., Private communication.

[16] Ross, A. J., "Investigation of Non-Linear Motion Experienced on a Slender Wing Research Aircraft, *Journal of Aircraft*, Vol. 9, September 1972.

[17] Visser, K. D. and Nelson, R. C., "Measurements of Circulation and Vorticity in the Leading Edge Vortex of a Delta Wing", *AIAA Journal*, September, 1991.

[18] Wong, G., "Experiments in the Control of Wing Rock at High Angles of Attack Using Tangential Leading Edge Blowing", Ph.D. Thesis, Department of Aeronautics & Astronautics, Stanford University, 1992.

Figures

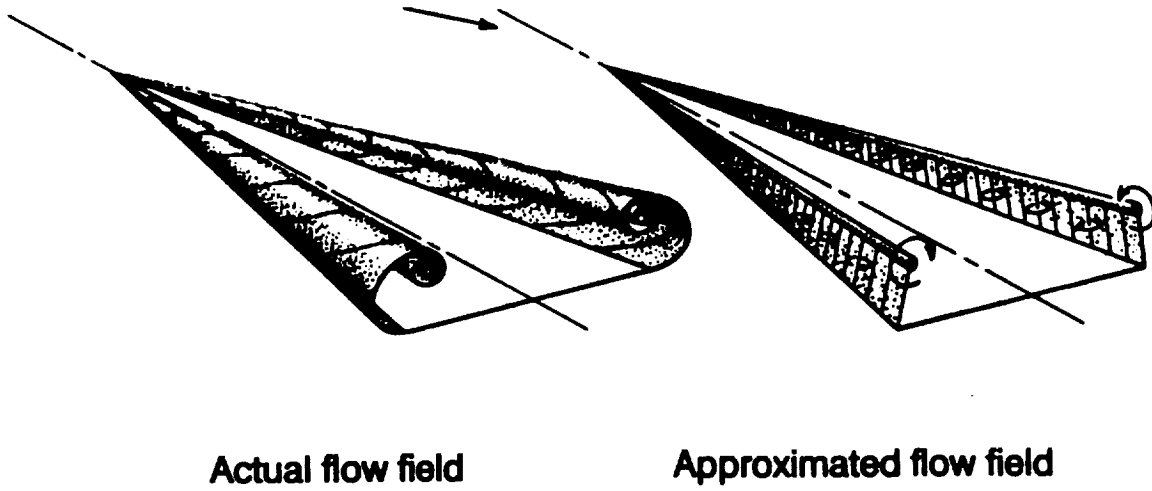


Figure 1. Actual and Approximated Flow Fields

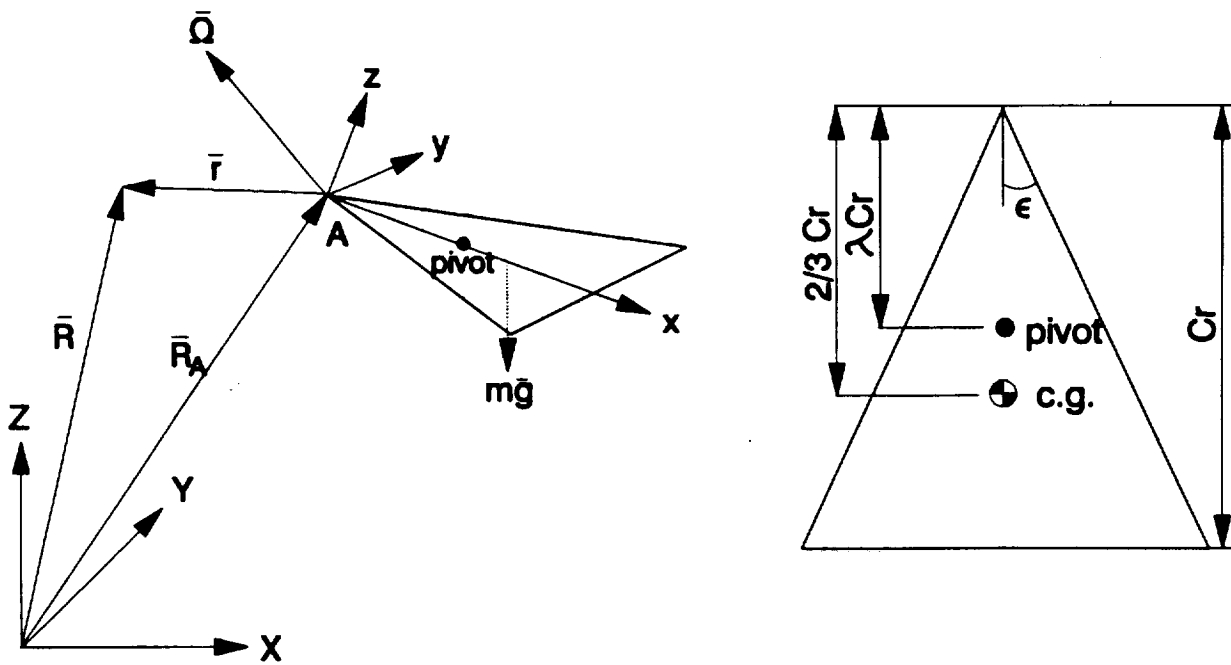


Figure 2. Schematic of the Delta Wing and Coordinate System

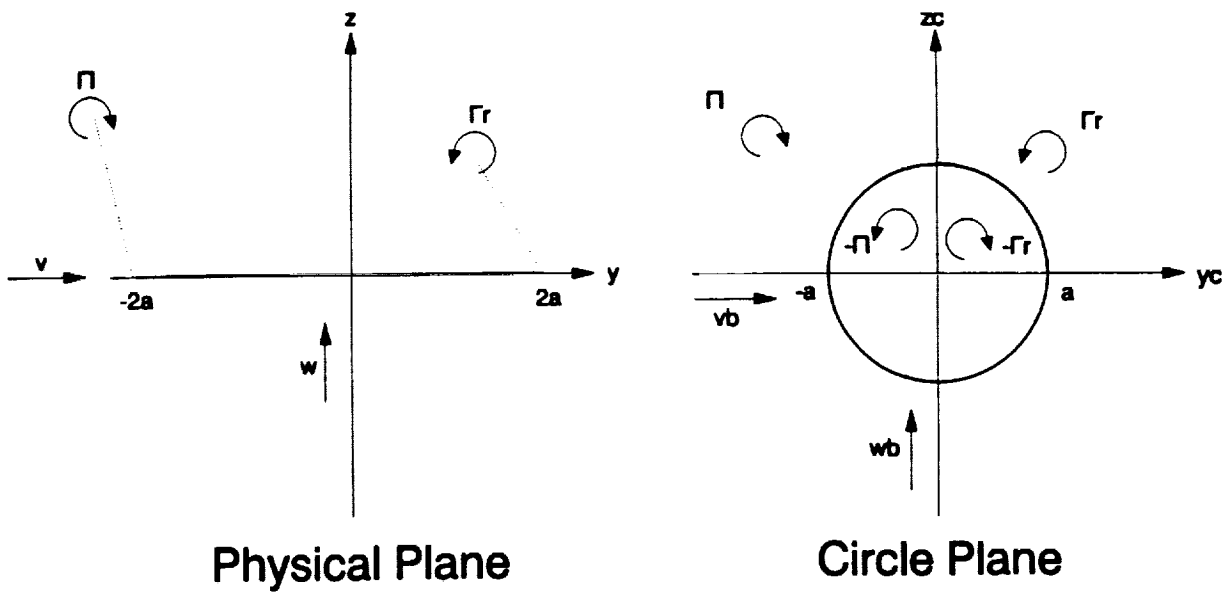


Figure 3. Sketch of Physical and Circle Plane

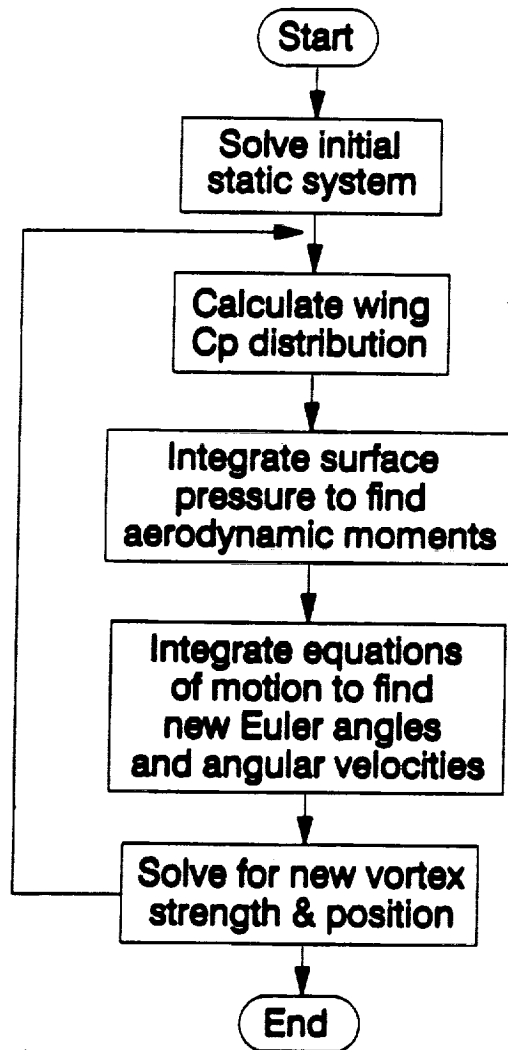


Figure 4. Flow Chart for Dynamic Simulation

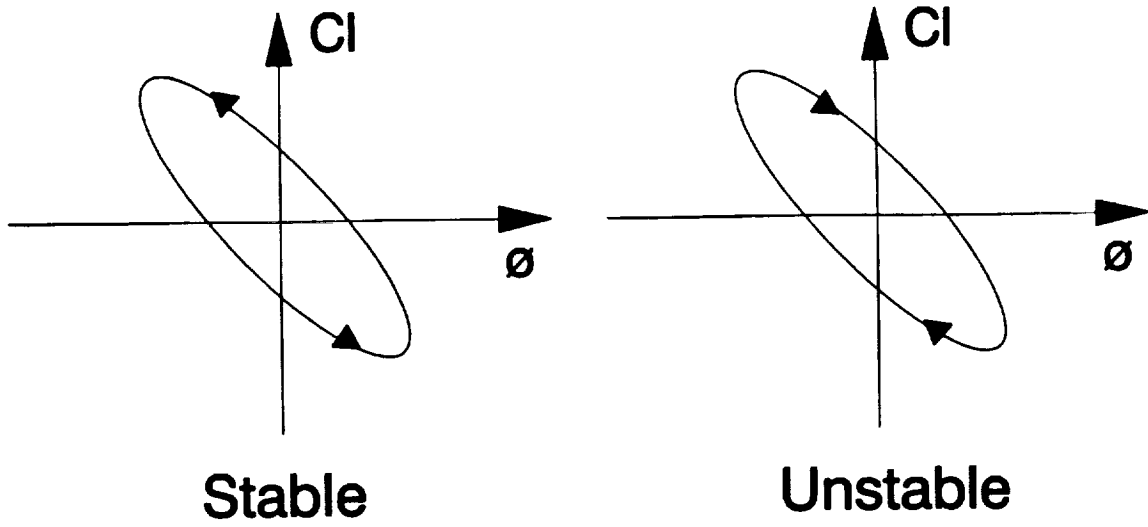


Figure 5. Conceptual Stable and Unstable Roll Moment Trajectories

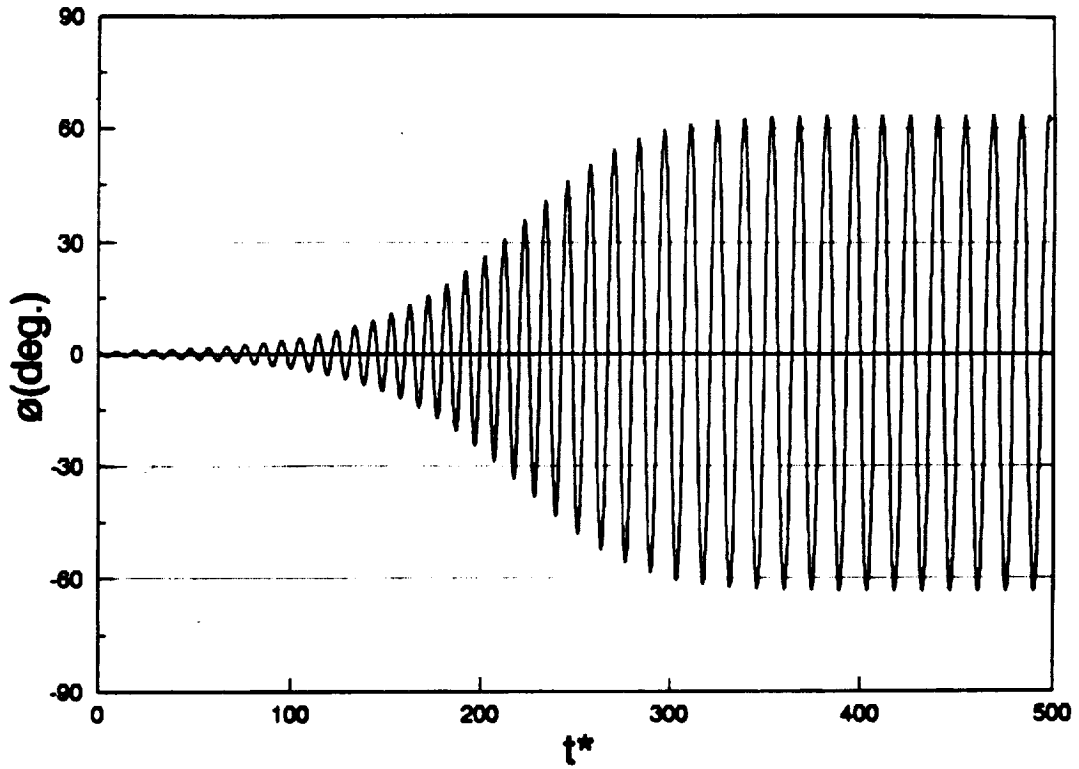


Figure 6(a). Wing Rock Time History ($\phi_0=0.5^\circ$, $\alpha=20^\circ$, $\beta=0^\circ$, $\epsilon=10^\circ$, $\delta=0\%$)

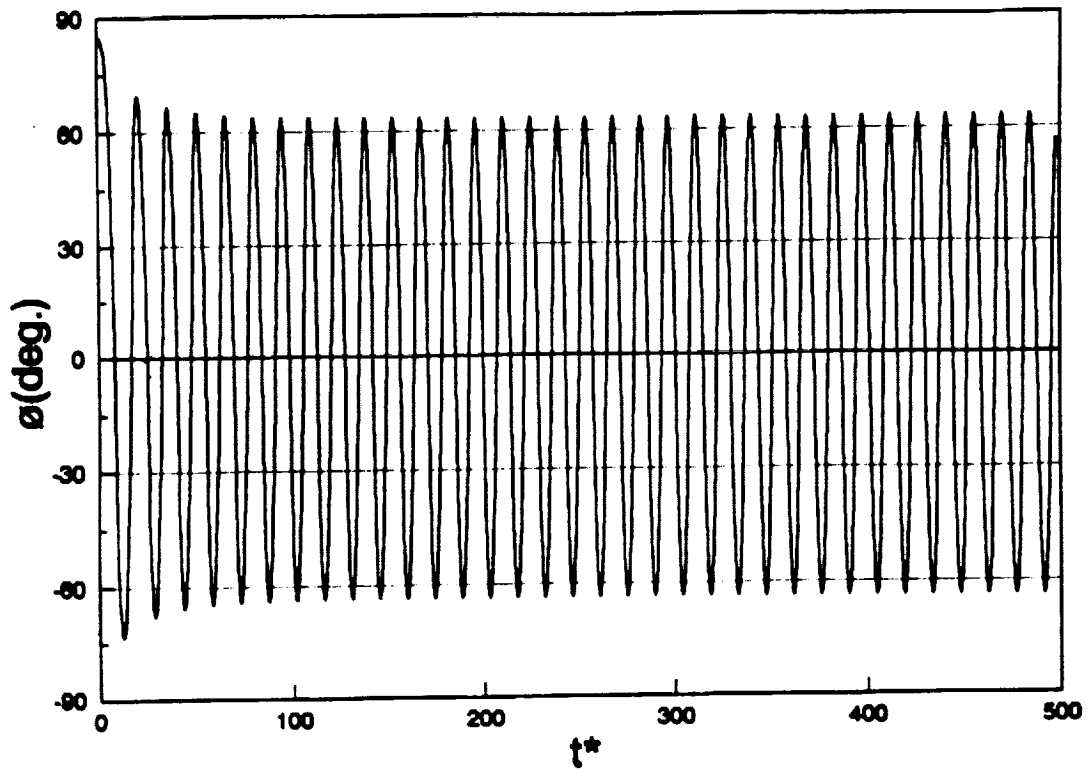


Figure 6(b). Wing Rock Time History ($\phi_0=85^\circ$, $\alpha=20^\circ$, $\beta=0^\circ$, $\epsilon=10^\circ$, $\delta=0\%$)

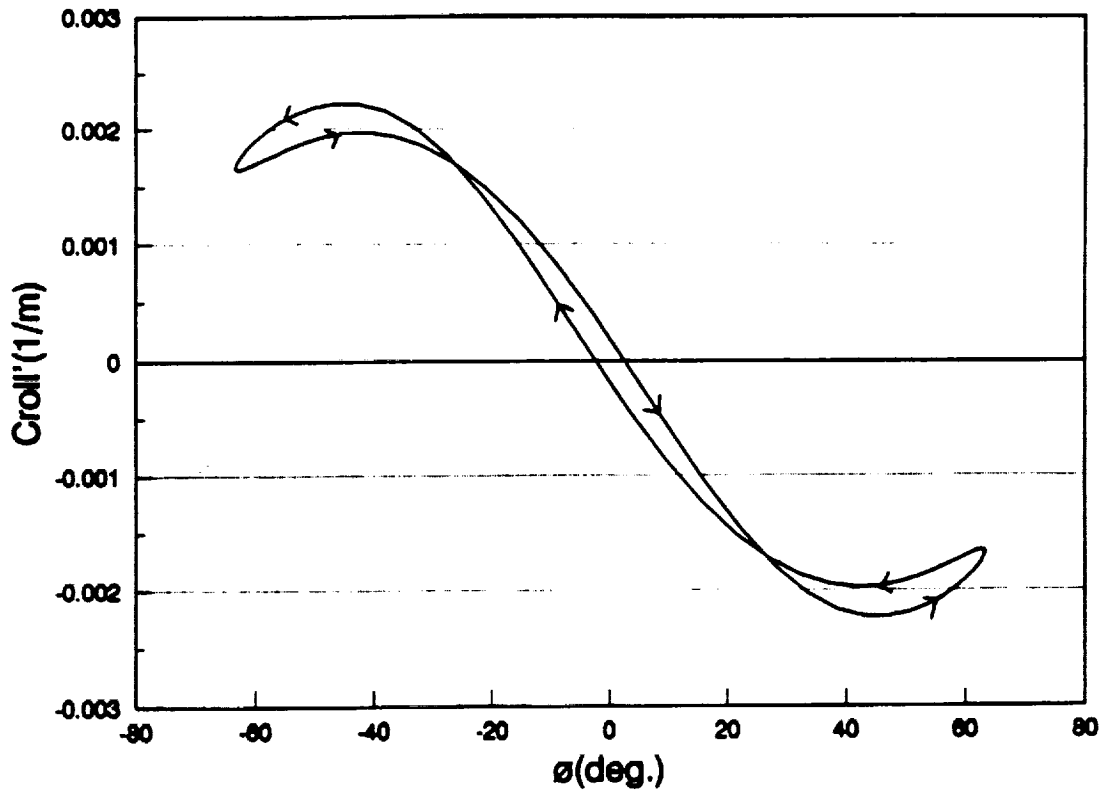


Figure 7(a). Total Sectional Roll Moment Coefficient ($\alpha=20^\circ$, $\beta=0^\circ$, $\epsilon=10^\circ$, $\delta=0\%$)

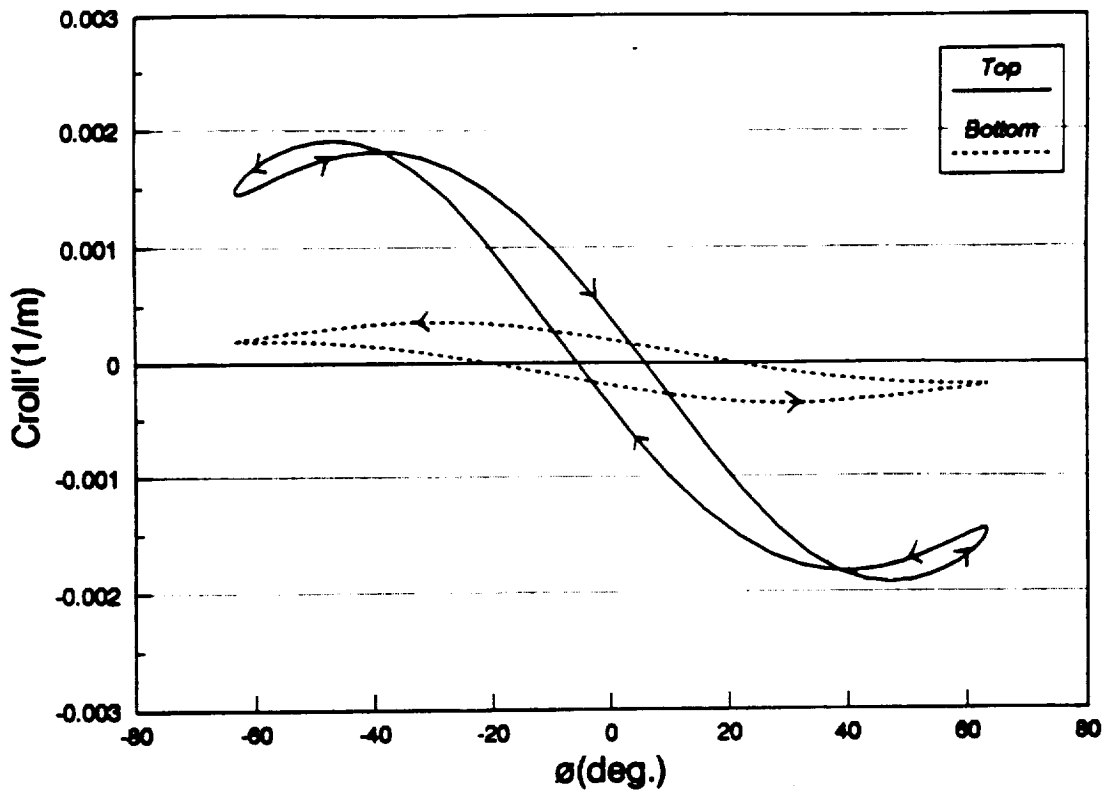


Figure 7(b). Top and Bottom Sectional Roll Moment Coefficient ($\alpha=20^\circ$, $\beta=0^\circ$, $\epsilon=10^\circ$, $\delta=0\%$)

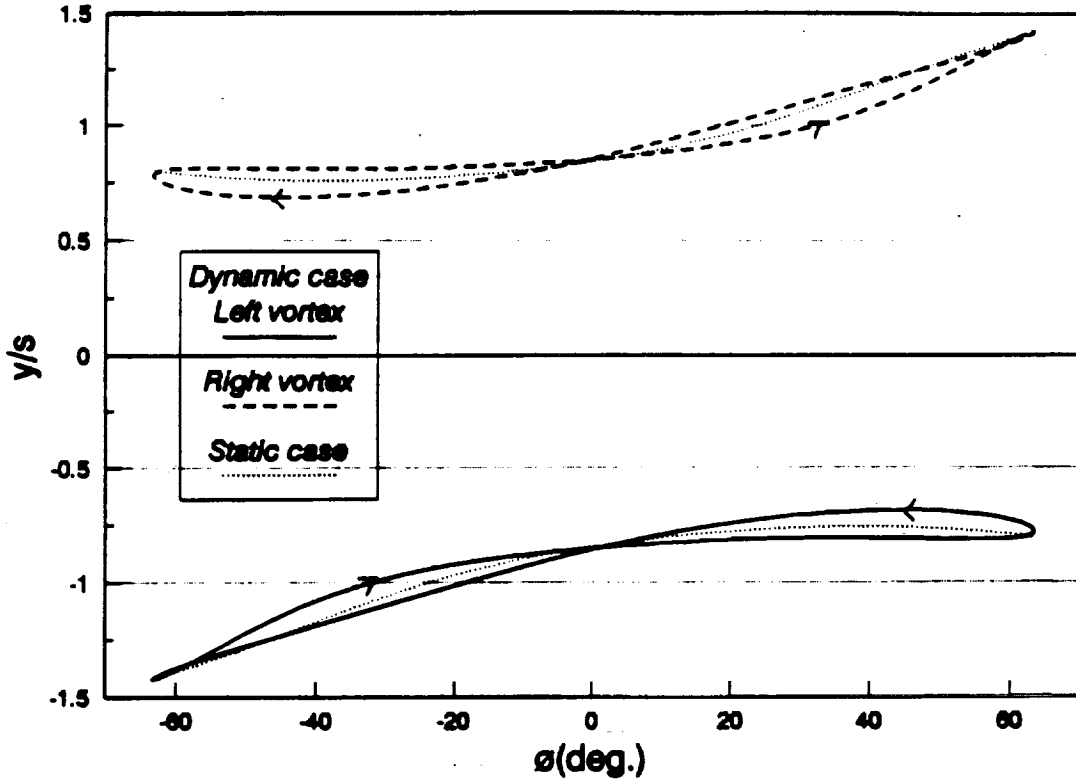


Figure 8(a). Spanwise Vortex Position During Wing Rock ($\alpha=20^\circ$, $\beta=0^\circ$, $\epsilon=10^\circ$, $\delta=0\%$)

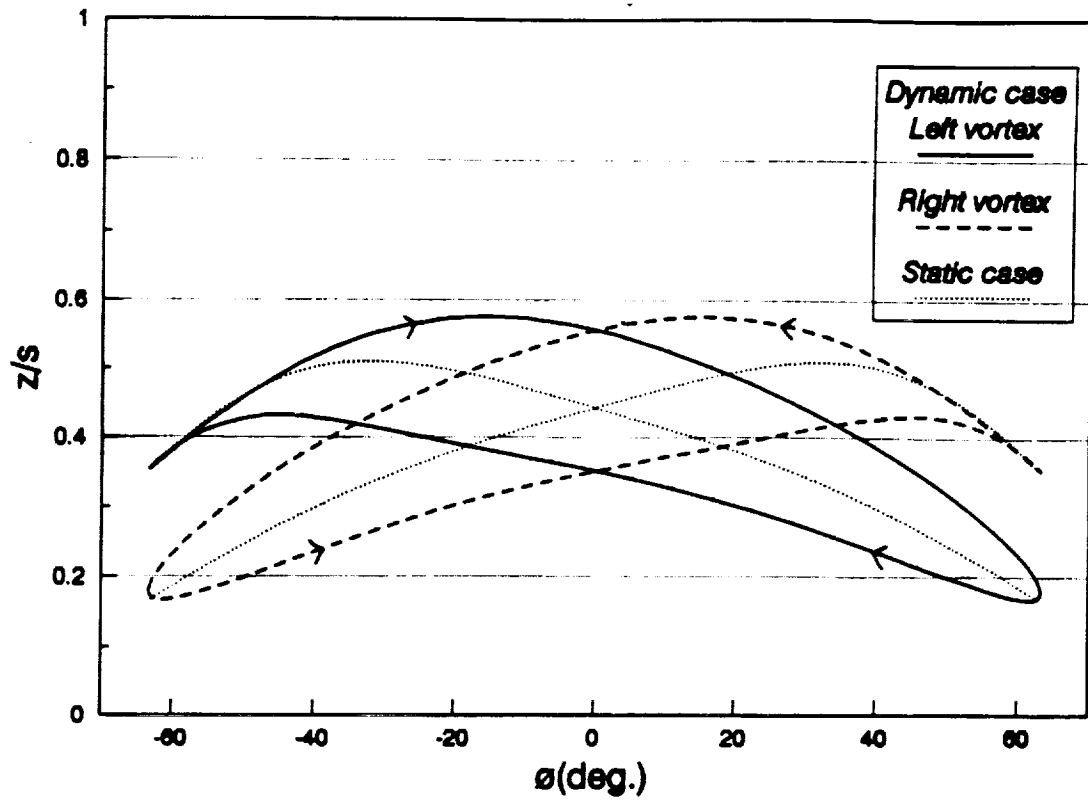


Figure 8(b). Normal Vortex Position During Wing Rock ($\alpha=20^\circ$, $\beta=0^\circ$, $\epsilon=10^\circ$, $\delta=0\%$)

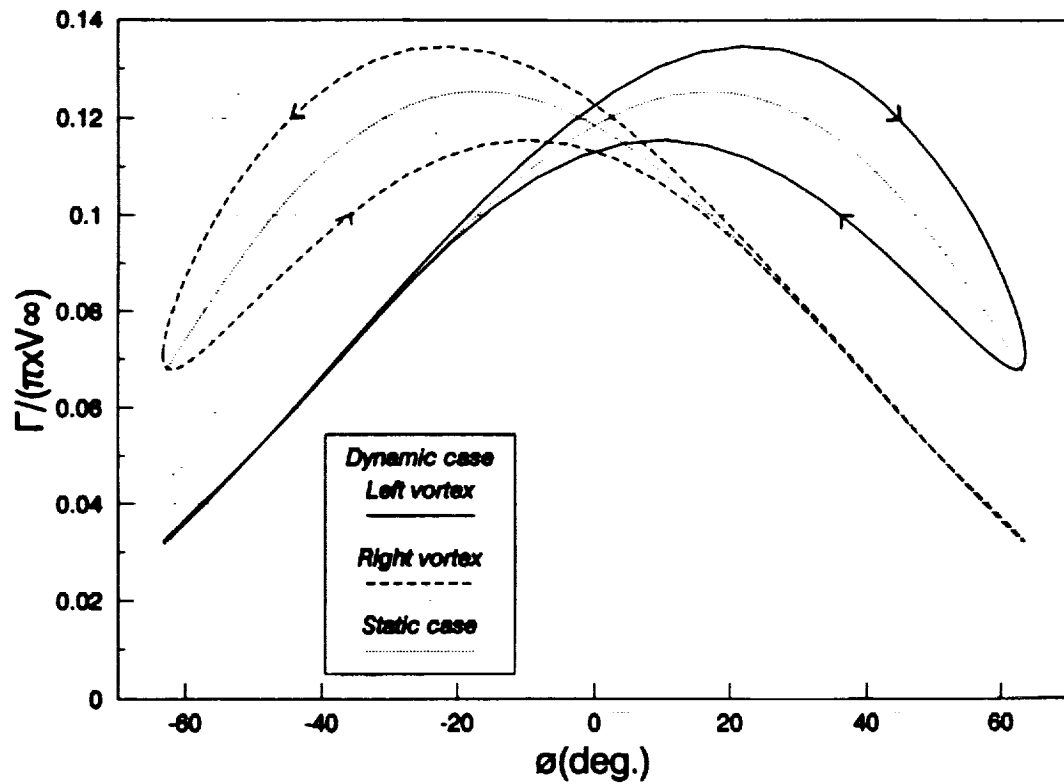


Figure 8(c). Unsteady Vortex Strength During Wing Rock ($\alpha=20^\circ$, $\beta=0^\circ$, $\epsilon=10^\circ$, $\delta=0\%$)

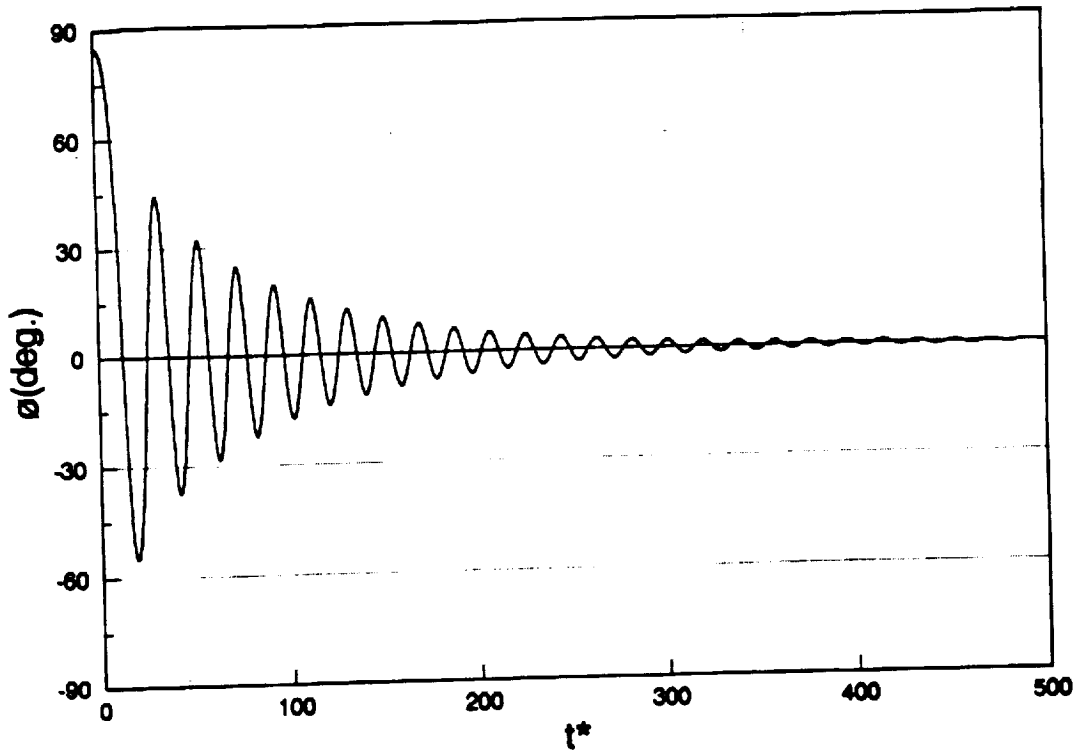


Figure 9. Wing Rock Time History ($\phi_0=85^\circ$, $\alpha=10^\circ$, $\beta=0^\circ$, $\epsilon=10^\circ$, $\delta=0\%$)

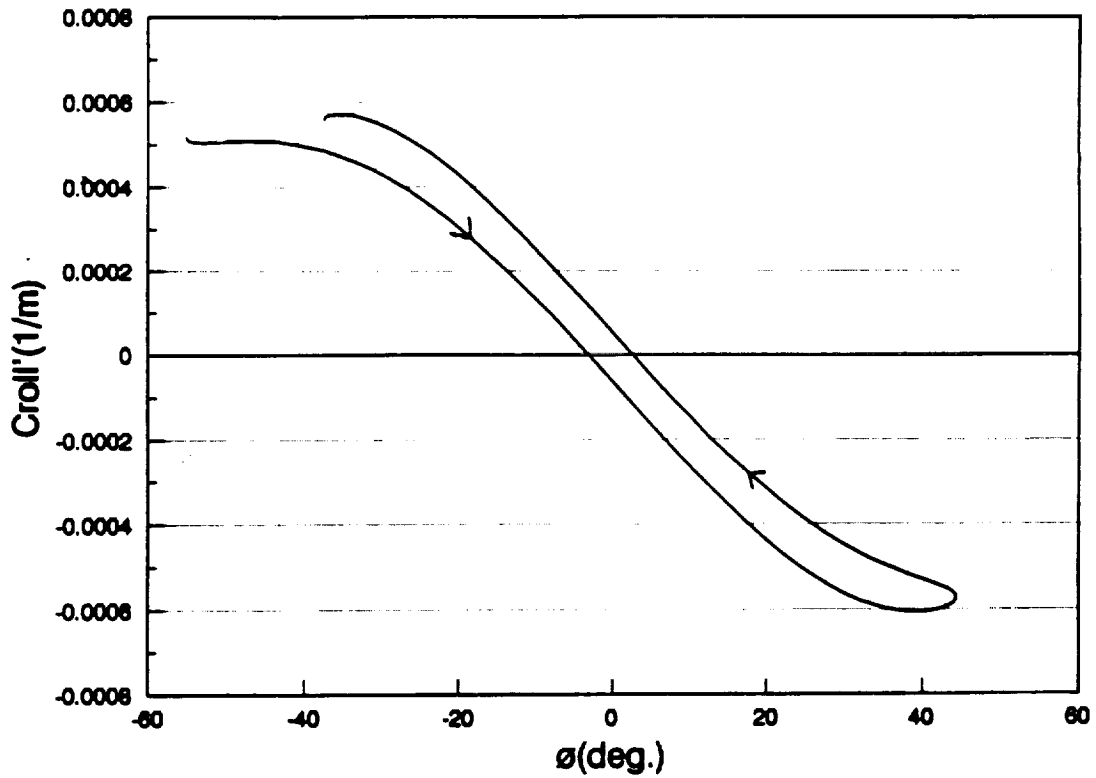


Figure 10(a). Total Sectional Roll Moment Coefficient ($\alpha=10^\circ$, $\beta=0^\circ$, $\epsilon=10^\circ$, $\delta=0\%$)

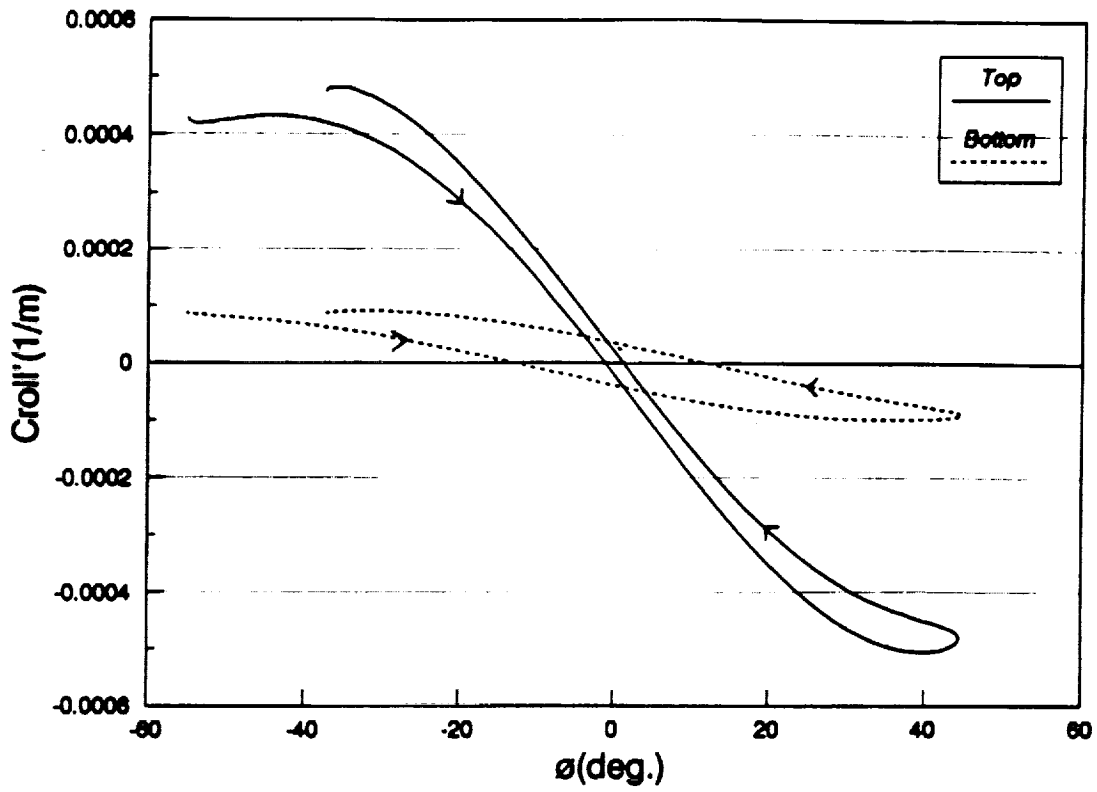


Figure 10(b). Top and Bottom Sectional Roll Moment Coefficient ($\alpha=10^\circ$, $\beta=0^\circ$, $\epsilon=10^\circ$, $\delta=0\%$)

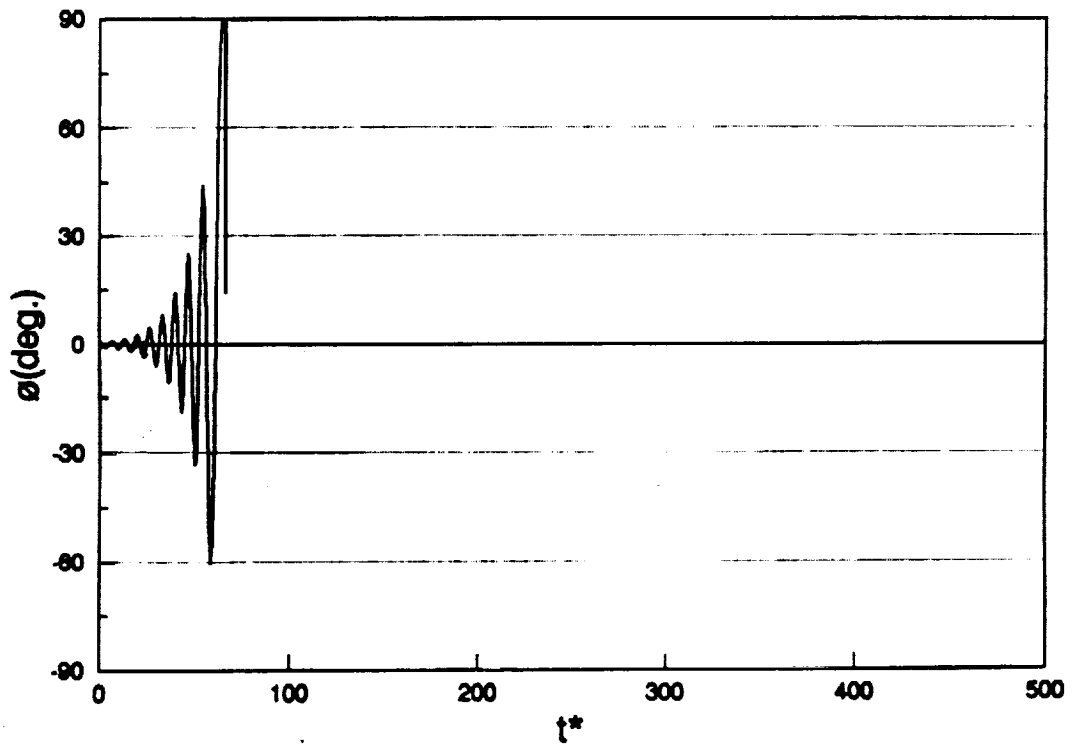


Figure 11. Wing Rock Time History ($\phi_0=0.5^\circ$, $\alpha=30^\circ$, $\beta=0^\circ$, $\epsilon=10^\circ$, $\delta=0\%$)

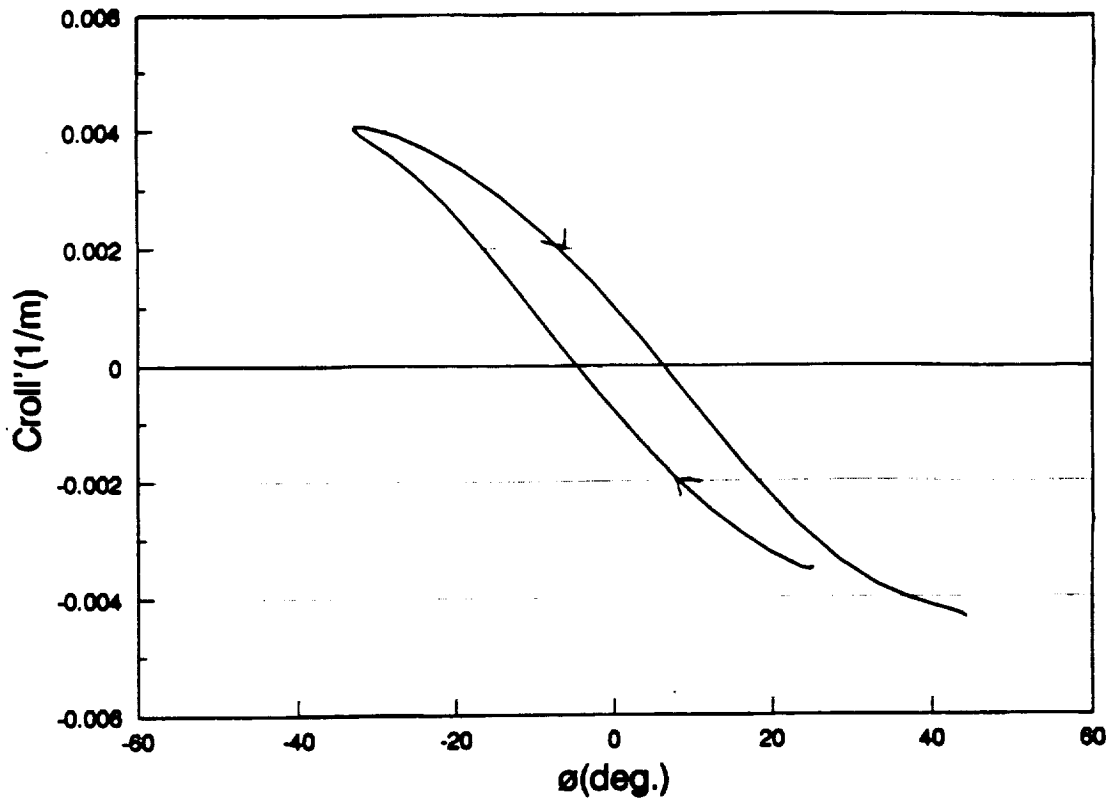


Figure 12(a). Total Sectional Roll Moment Coefficient ($\alpha=30^\circ$, $\beta=0^\circ$, $\epsilon=10^\circ$, $\delta=0\%$)

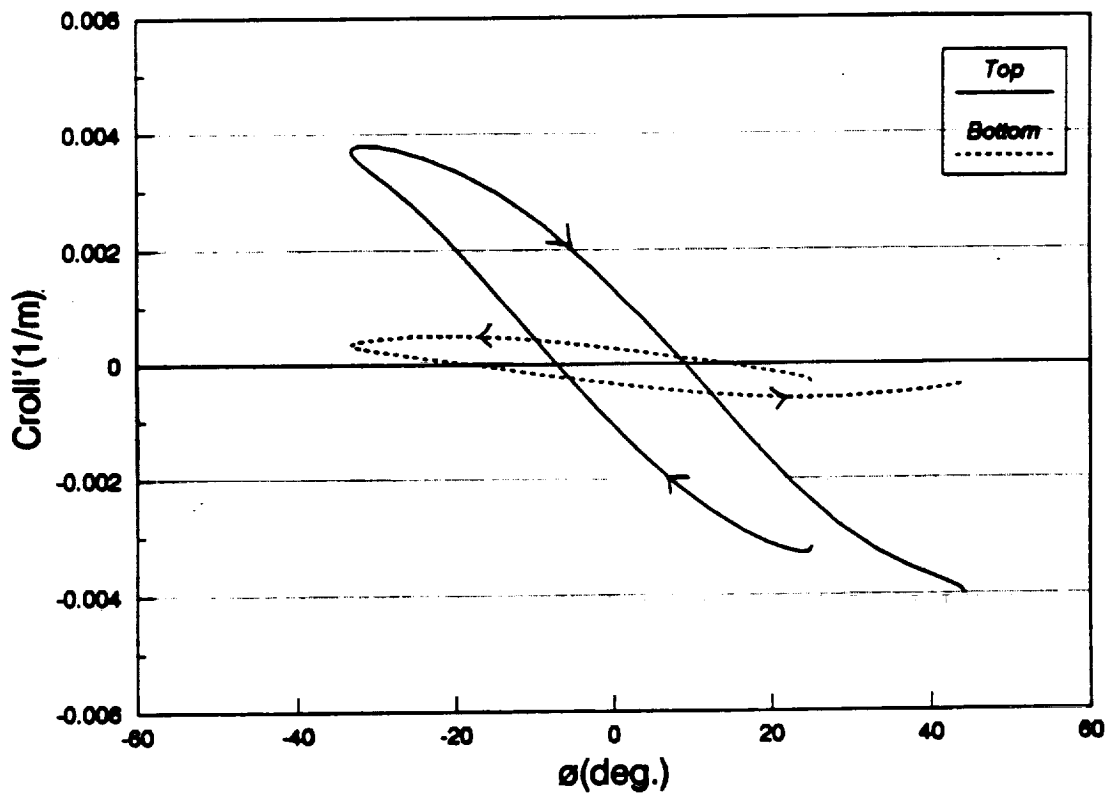


Figure 12(b). Top and Bottom Sectional Roll Moment Coefficient ($\alpha=30^\circ$, $\beta=0^\circ$, $\epsilon=10^\circ$, $\delta=0\%$)

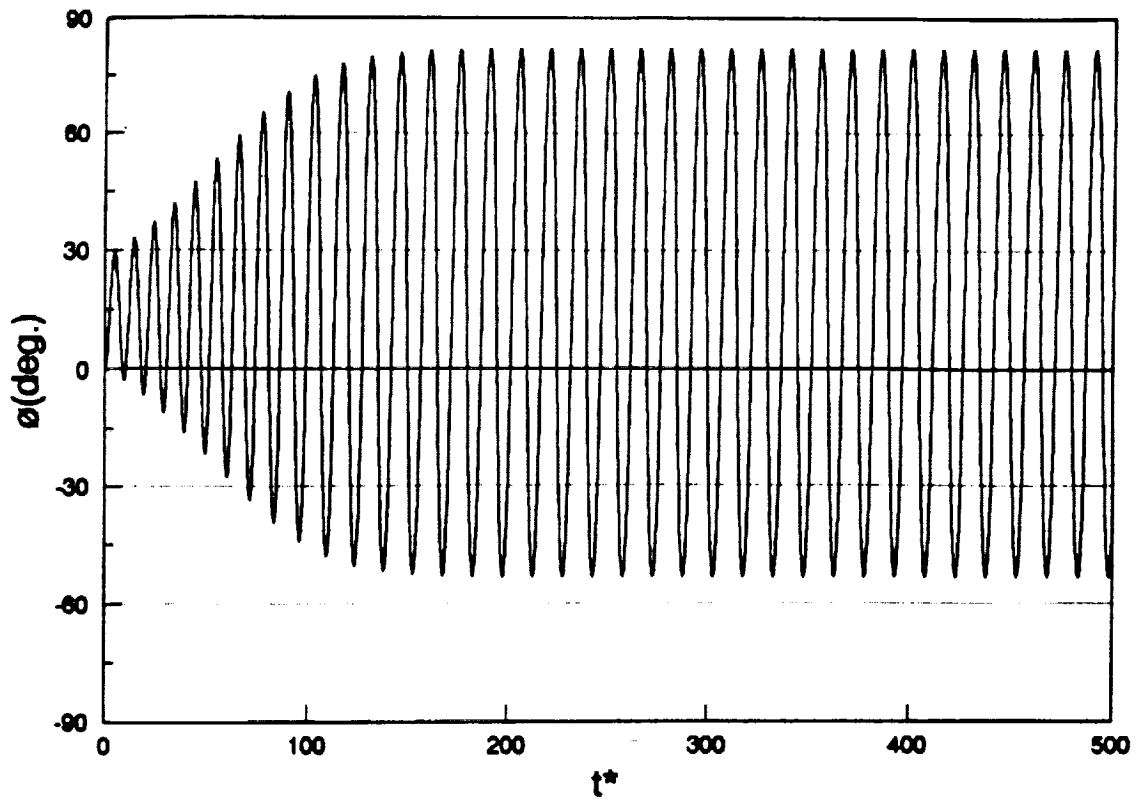


Figure 13(a). Wing Rock Time History ($\phi_0=0.5^\circ$, $\alpha=20^\circ$, $\beta=5^\circ$, $\epsilon=10^\circ$, $\delta=0\%$)

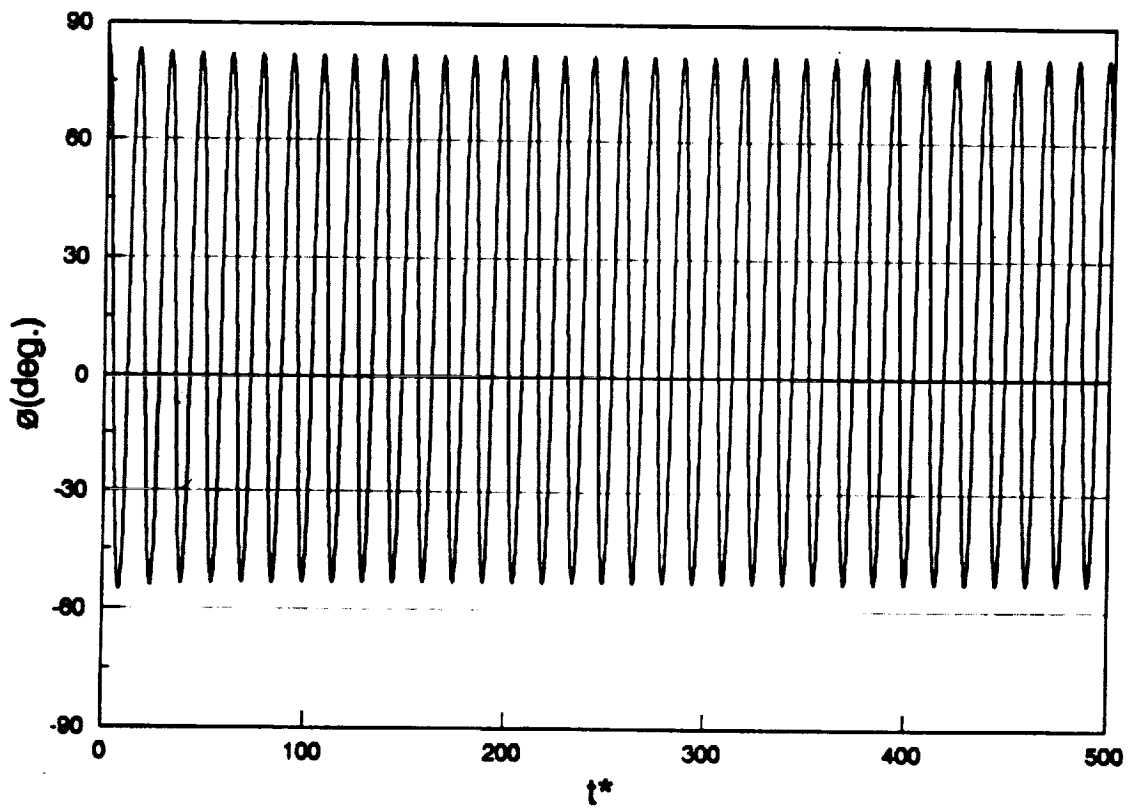


Figure 13(b). Wing Rock Time History ($\phi_0=85^\circ$, $\alpha=20^\circ$, $\beta=5^\circ$, $\epsilon=10^\circ$, $\delta=0\%$)

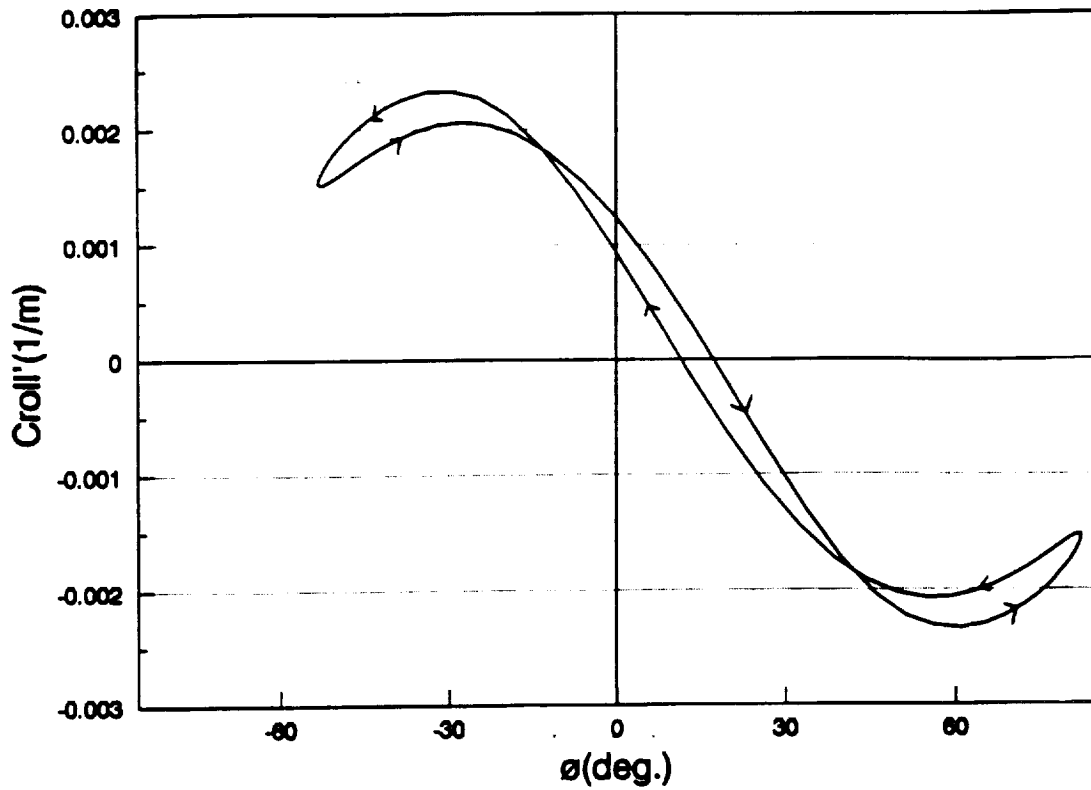


Figure 14(a). Total Sectional Roll Moment Coefficient ($\alpha=20^\circ$, $\beta=5^\circ$, $\epsilon=10^\circ$, $\delta=0\%$)

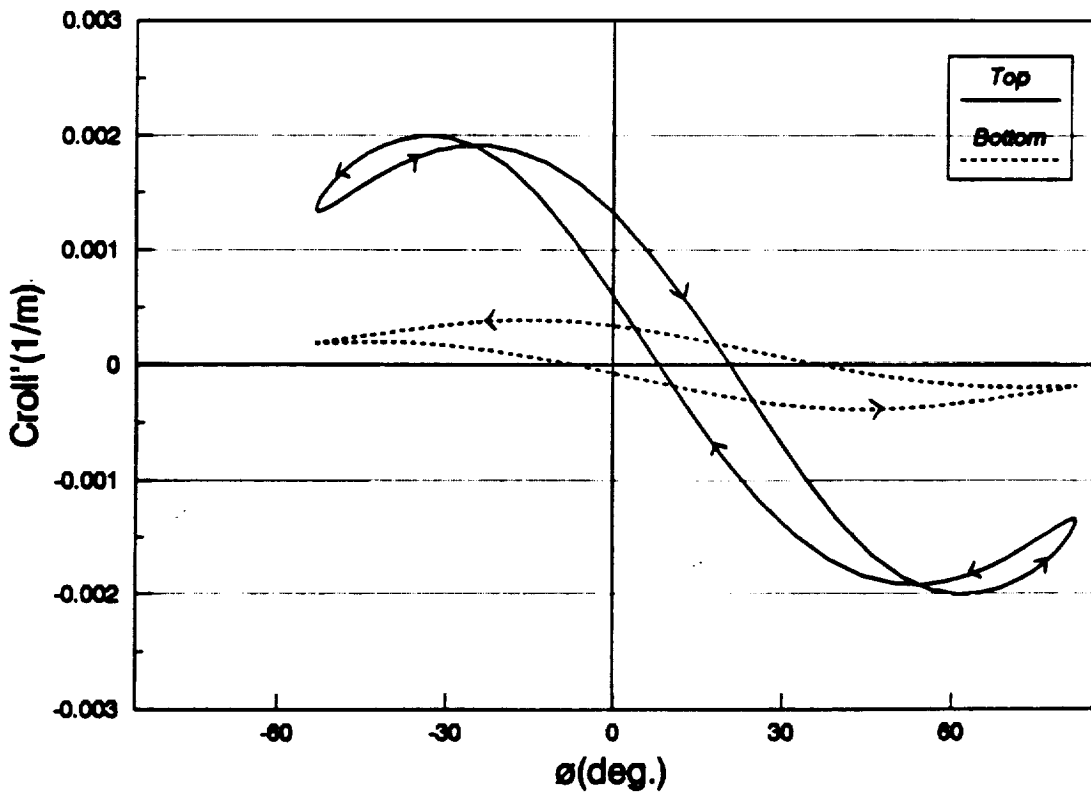


Figure 14(b). Top and Bottom Sectional Roll Moment Coefficient ($\alpha=20^\circ$, $\beta=5^\circ$, $\epsilon=10^\circ$, $\delta=0\%$)

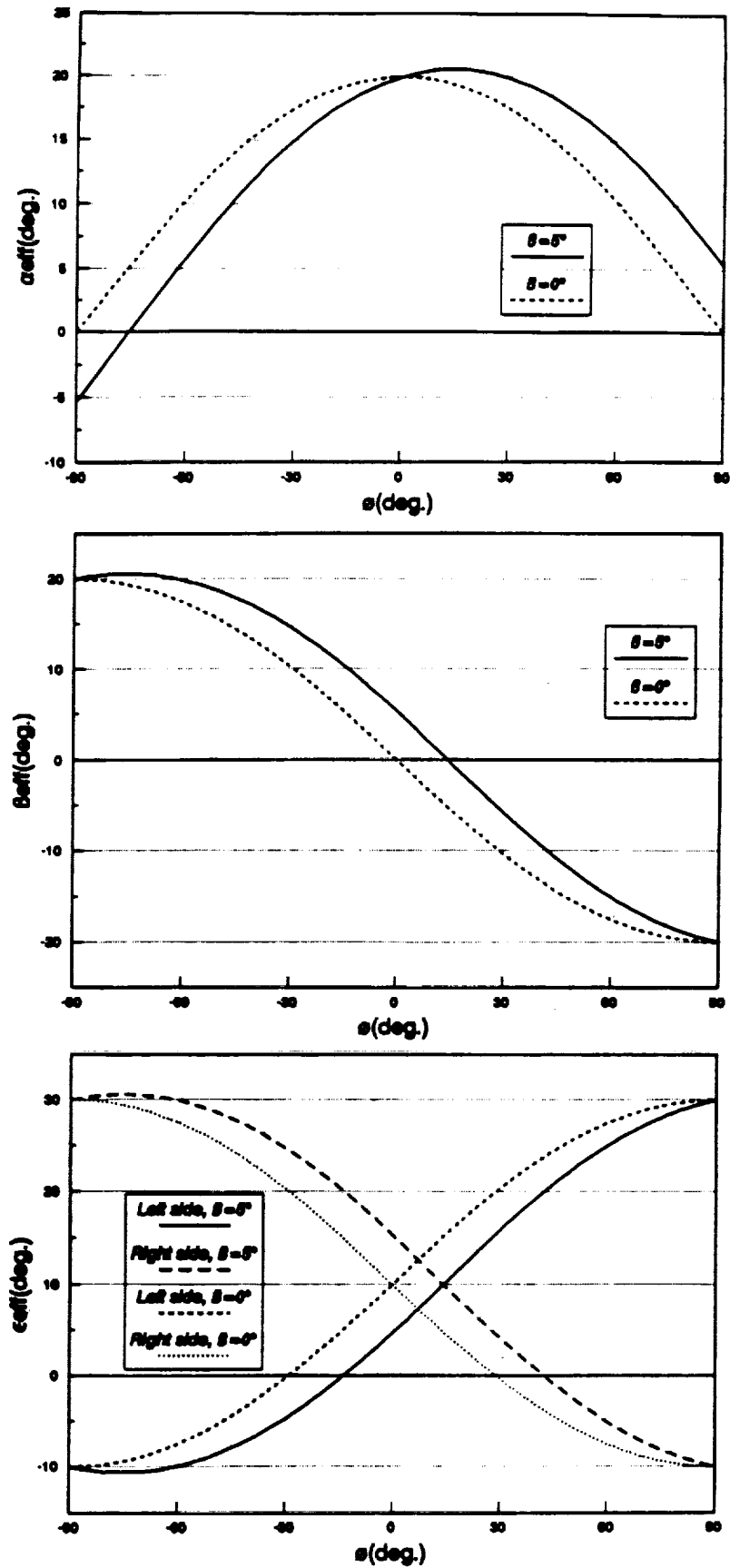


Figure 15. Effective Angle of Attack, Yaw Angle and Semi-Apex Angle as a Function of Roll Angle for $\beta=0^\circ$ and $\beta=5^\circ$

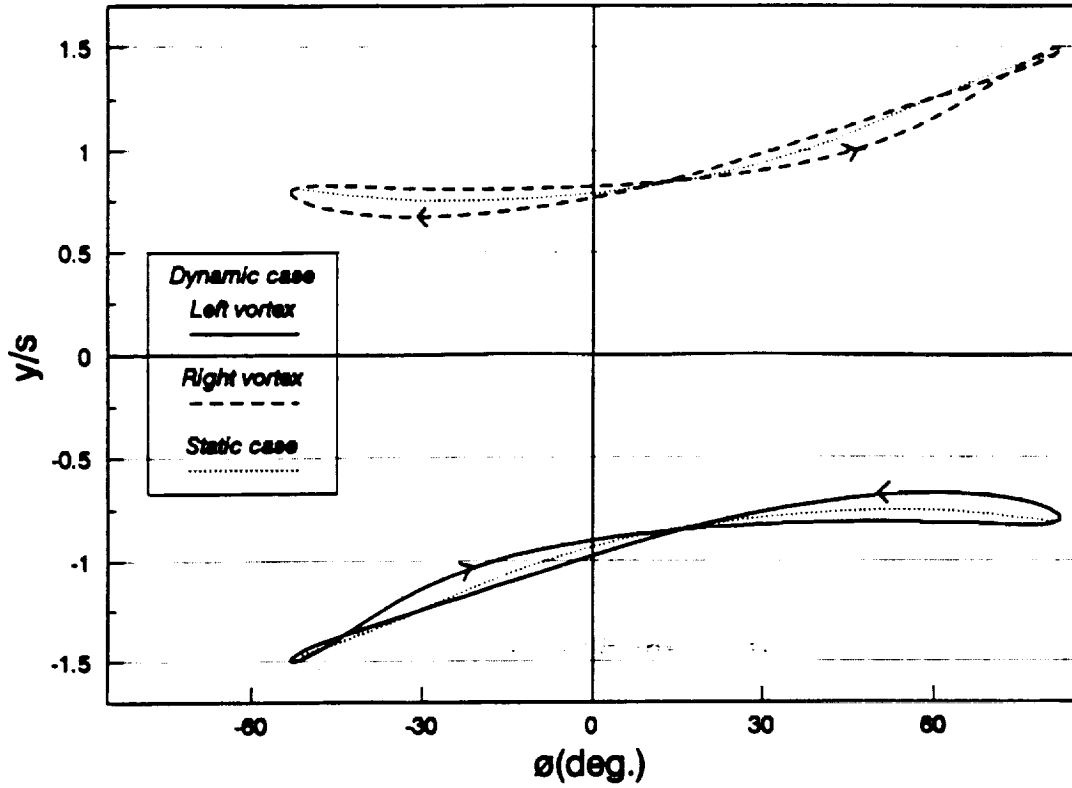


Figure 16(a). Spanwise Vortex Position During Wing Rock ($\alpha=20^\circ$, $\beta=5^\circ$, $\epsilon=10^\circ$, $\delta=0\%$)

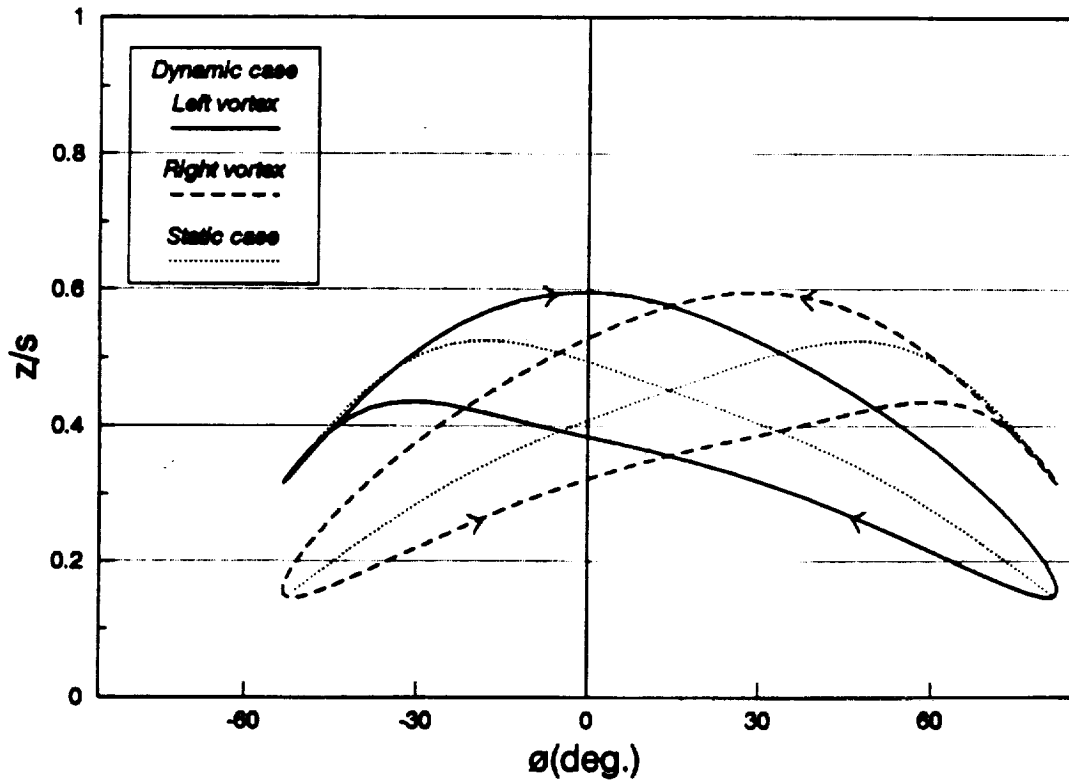


Figure 16(b). Normal Vortex Position During Wing Rock ($\alpha=20^\circ$, $\beta=5^\circ$, $\epsilon=10^\circ$, $\delta=0\%$)

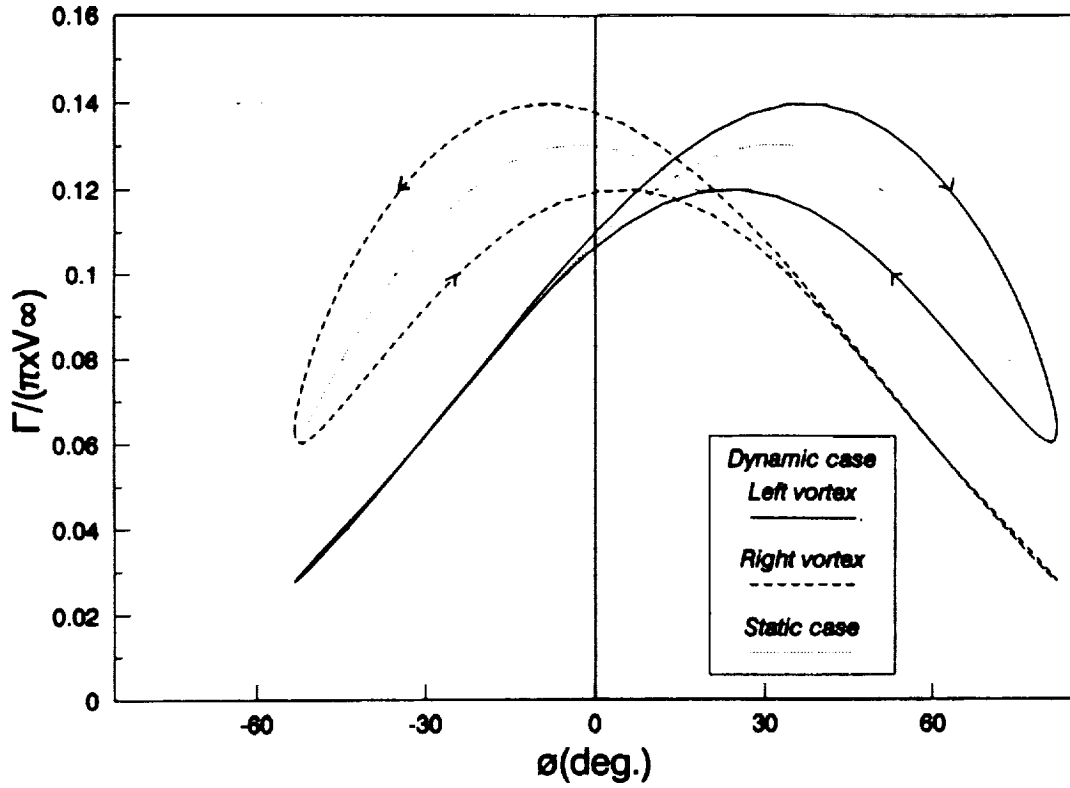


Figure 16(c). Unsteady Vortex Strength During Wing Rock ($\alpha=20^\circ$, $\beta=5^\circ$, $\epsilon=10^\circ$, $\delta=0\%$)

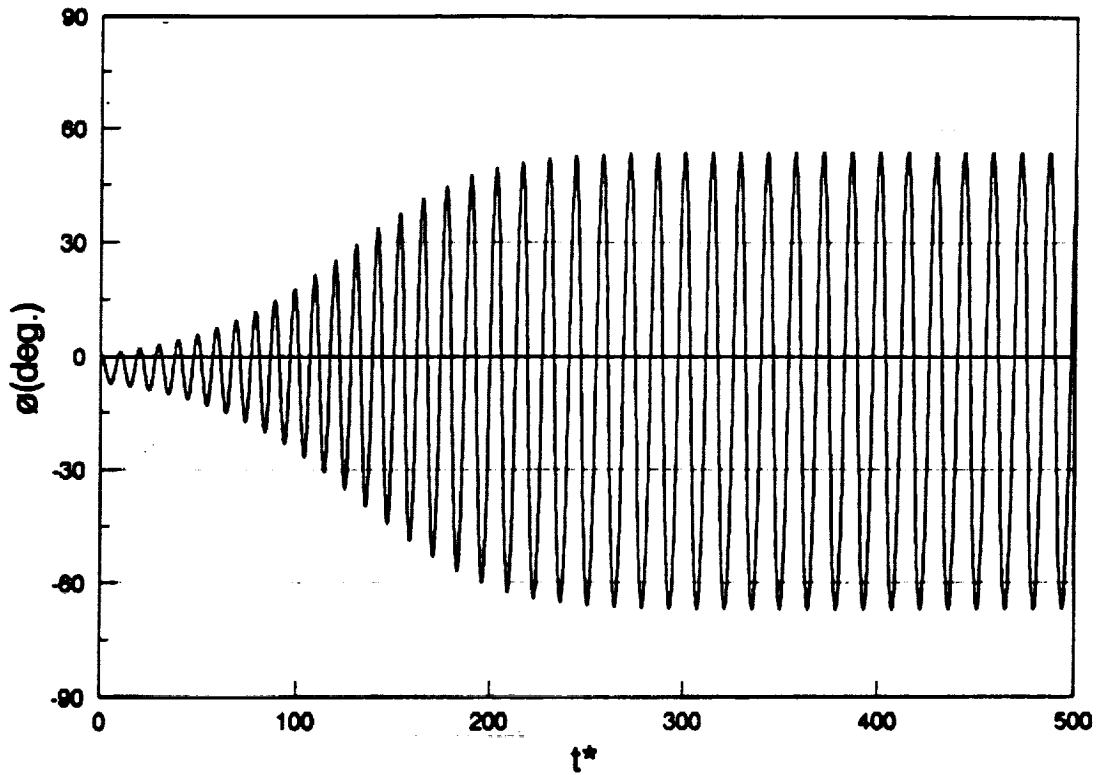


Figure 17(a). Wing Rock Time History ($\phi_0=0.5^\circ$, $\alpha=20^\circ$, $\beta=0^\circ$, $\epsilon=10^\circ$, $\delta_1=0\%$, $\delta_r=1\%$)

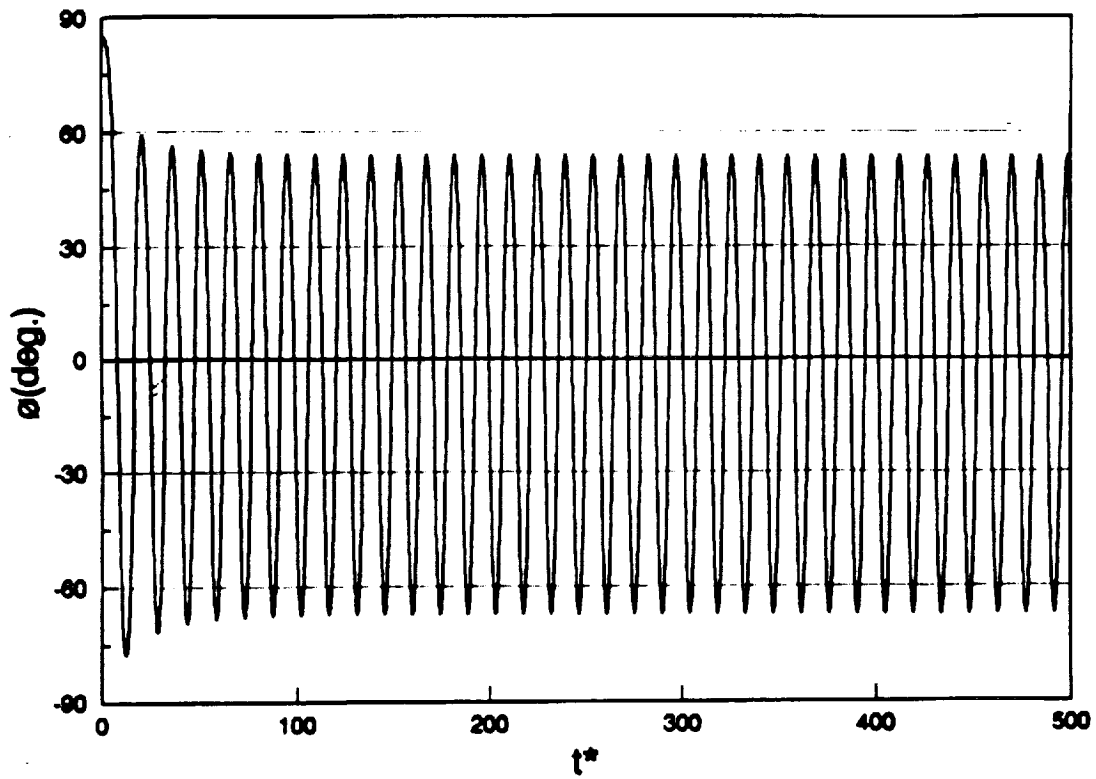


Figure 17(b). Wing Rock Time History ($\phi_0=85^\circ$, $\alpha=20^\circ$, $\beta=0^\circ$, $\epsilon=10^\circ$, $\delta_l=0\%$, $\delta_r=1\%$)

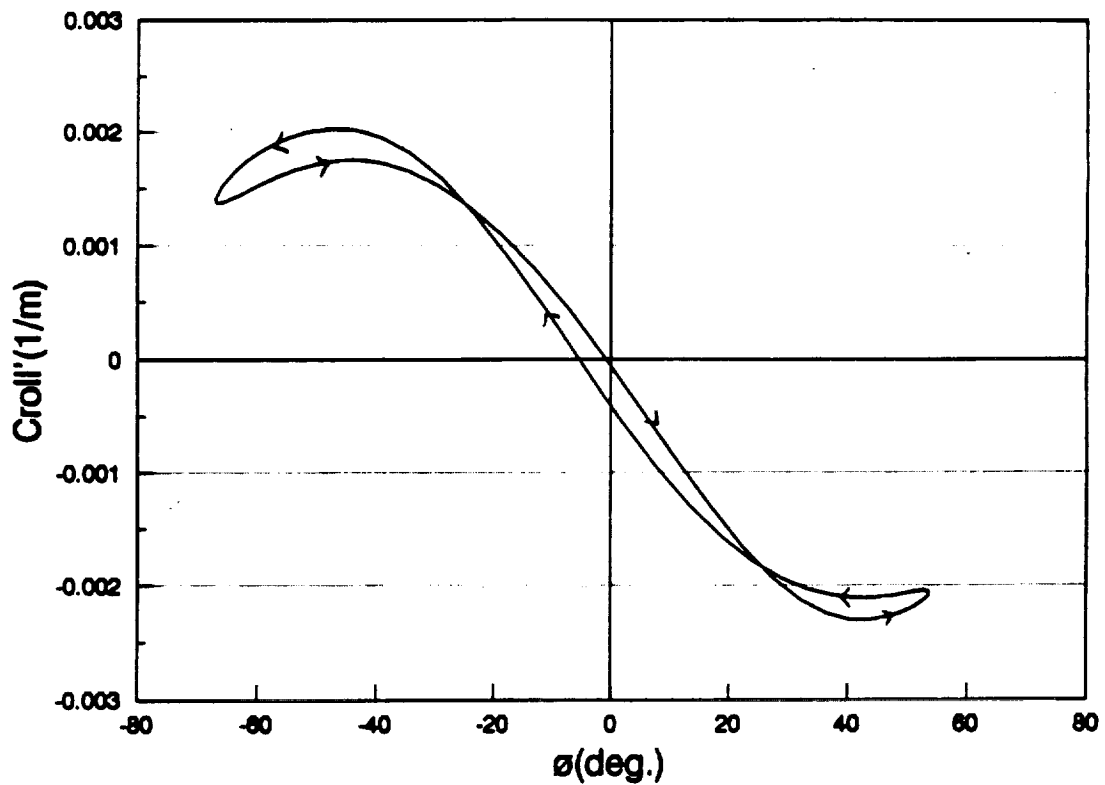


Figure 18(a). Total Sectional Roll Moment Coefficient ($\alpha=20^\circ$, $\beta=0^\circ$, $\epsilon=10^\circ$, $\delta_l=0\%$, $\delta_r=1\%$)

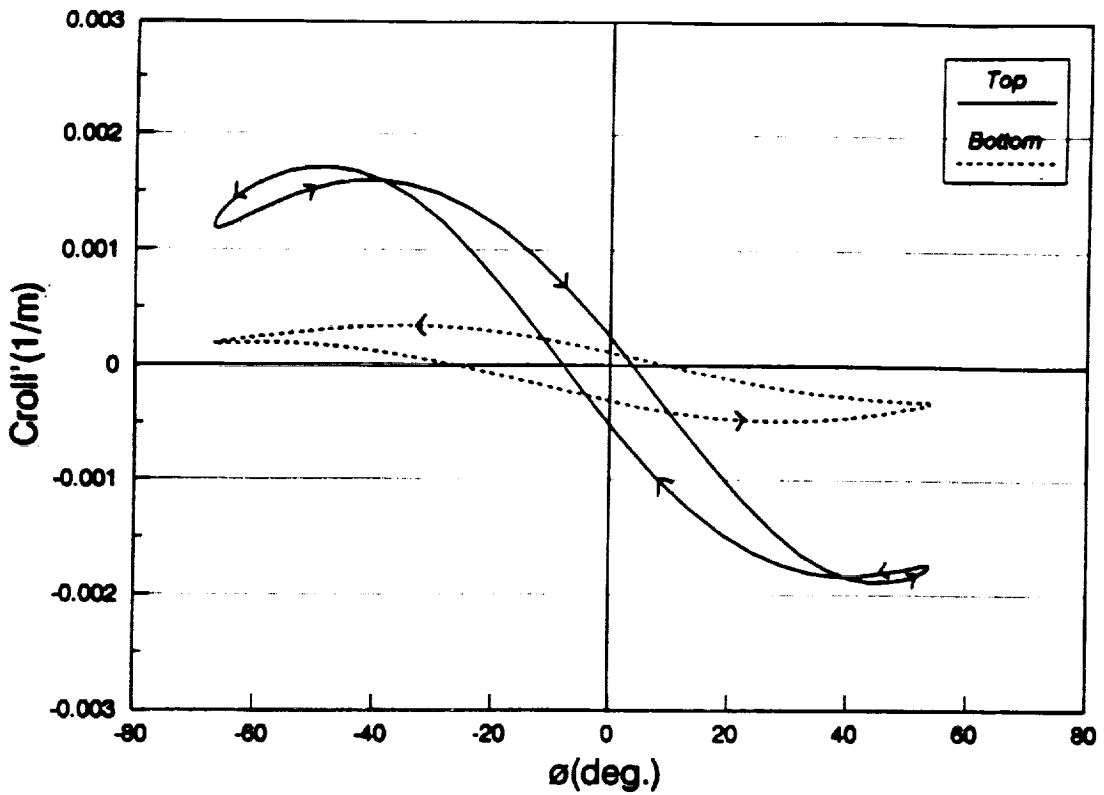


Figure 18(b). Top and Bottom Sectional Roll Moment Coefficient ($\alpha=20^\circ$, $\beta=0^\circ$, $\epsilon=10^\circ$, $\delta_l=0\%$, $\delta_r=1\%$)

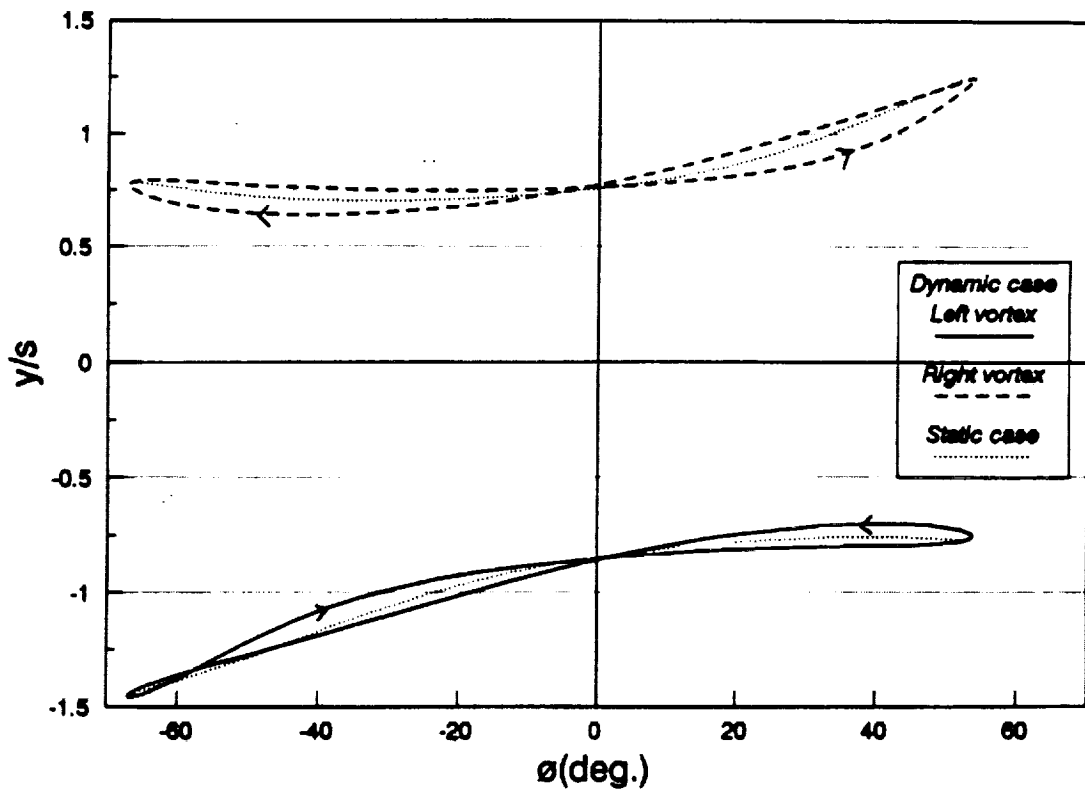


Figure 19(a). Spanwise Vortex Position During Wing Rock ($\alpha=20^\circ$, $\beta=0^\circ$, $\epsilon=10^\circ$, $\delta_l=0\%$, $\delta_r=1\%$)

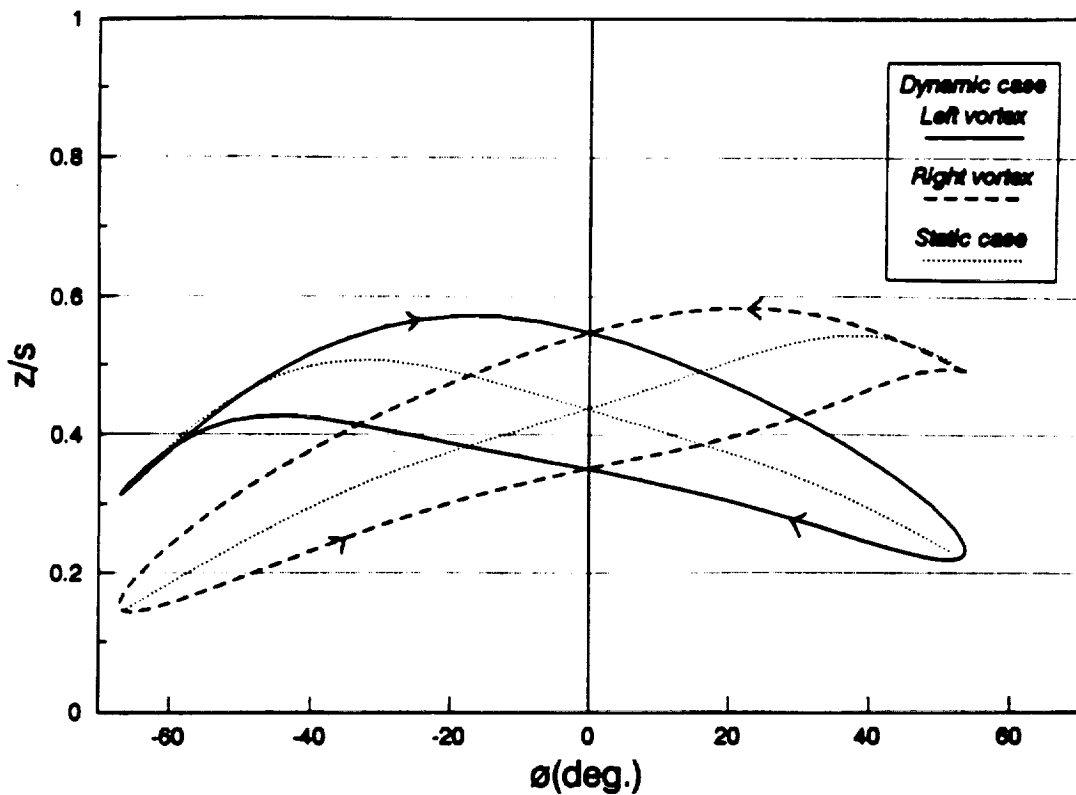


Figure 19(b). Normal Vortex Position During Wing Rock ($\alpha=20^\circ$, $\beta=0^\circ$, $\epsilon=10^\circ$, $\delta_l=0\%$, $\delta_r=1\%$)

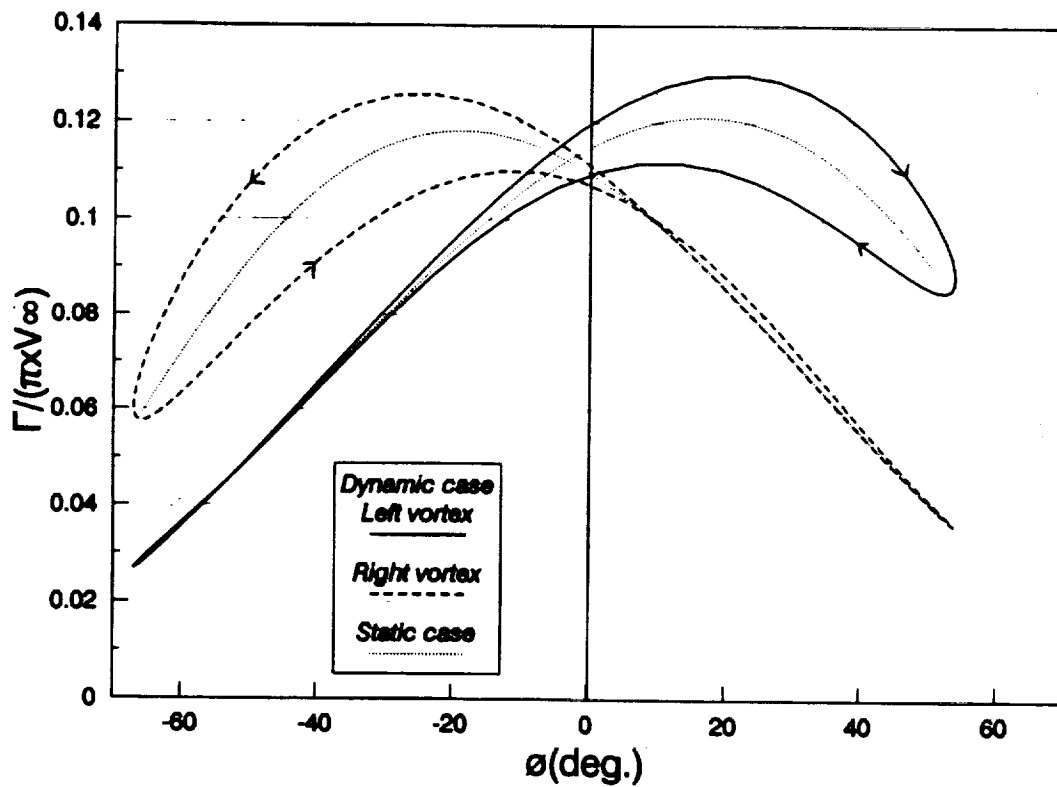


Figure 19(c). Unsteady Vortex Strength During Wing Rock ($\alpha=20^\circ$, $\beta=0^\circ$, $\epsilon=10^\circ$, $\delta_l=0\%$, $\delta_r=1\%$)

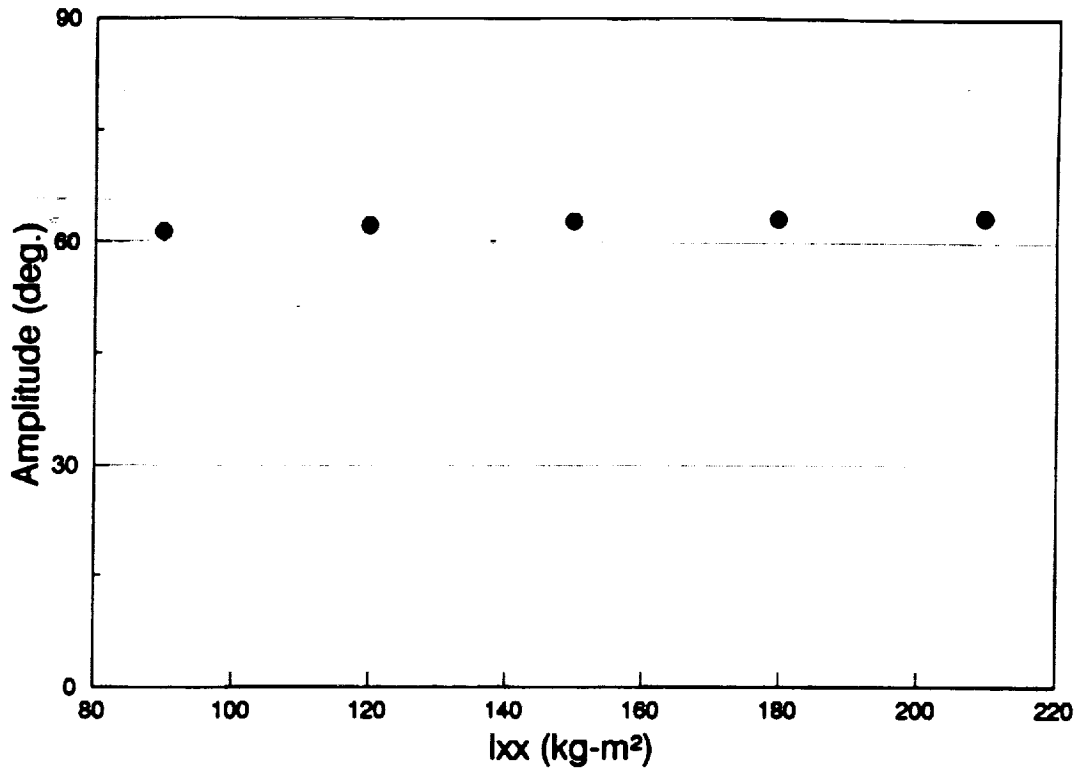


Figure 20(a). Effect of Inertia Variation on Wing Rock Amplitude ($\alpha=20^\circ$, $\beta=0^\circ$, $\epsilon=10^\circ$, $\delta=0\%$)

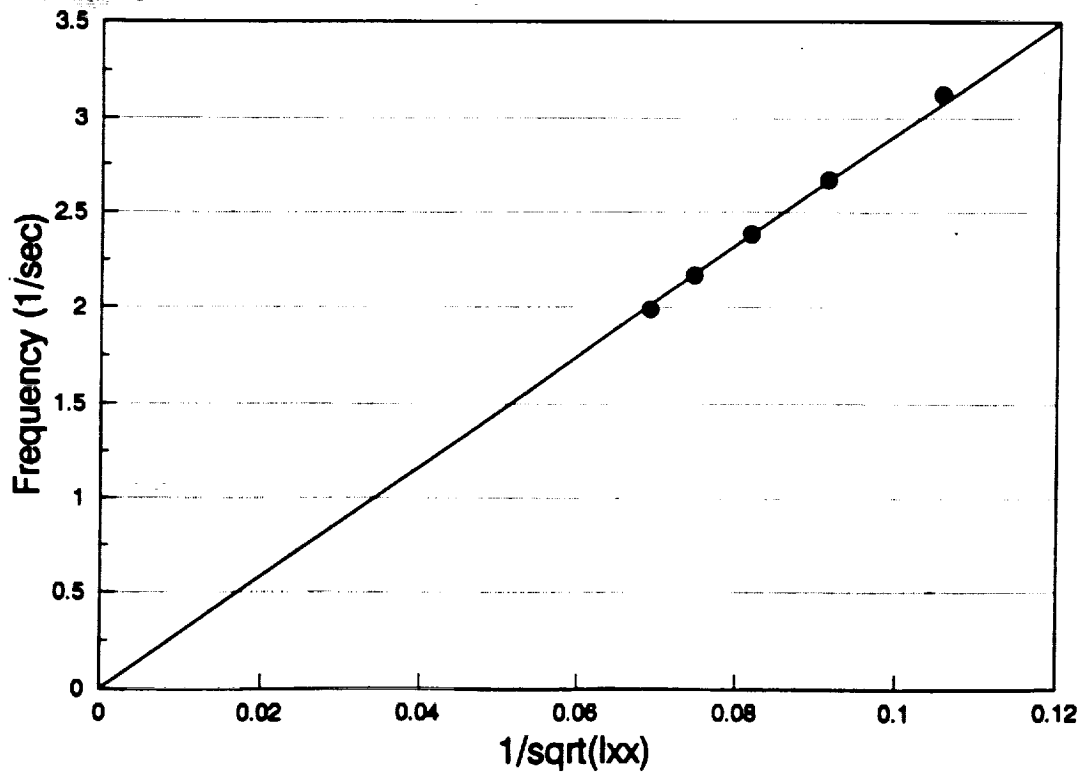


Figure 20(b). Effect of Inertia Variation on Wing Rock Frequency ($\alpha=20^\circ$, $\beta=0^\circ$, $\epsilon=10^\circ$, $\delta=0\%$)

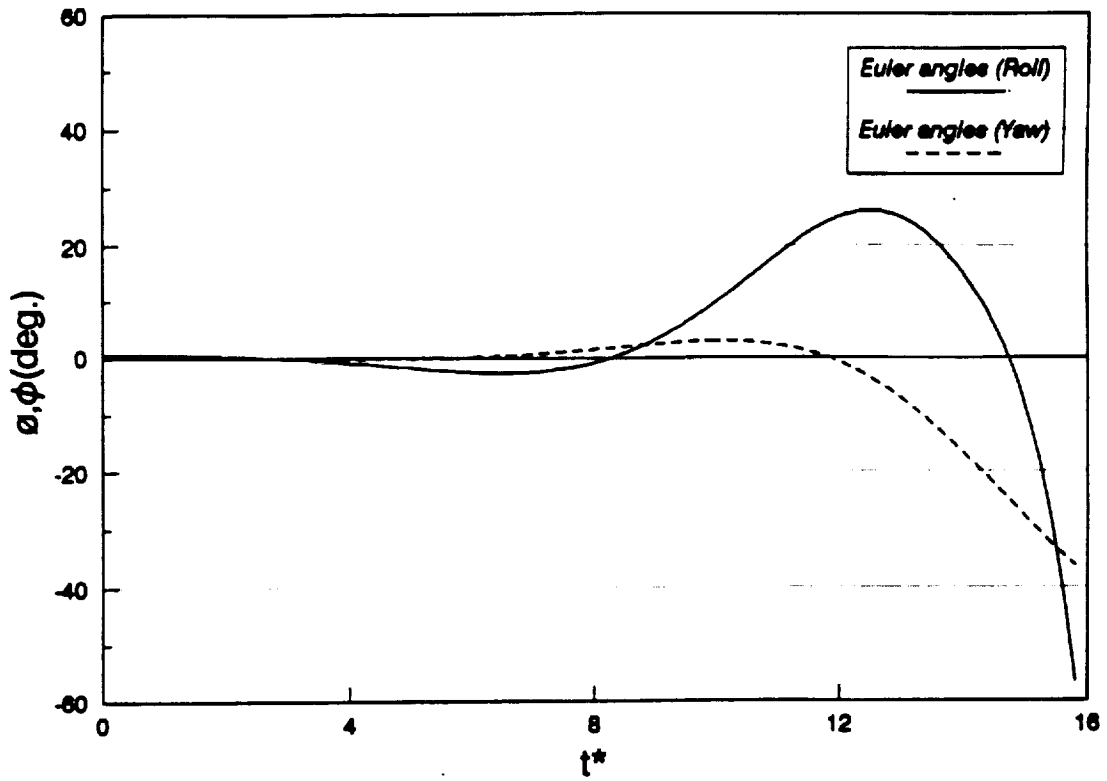


Figure 21(a). Row and Yaw Euler Angle Time History ($\alpha=10^\circ$, $\beta=0^\circ$, $\epsilon=5^\circ$, $\delta=0\%$)

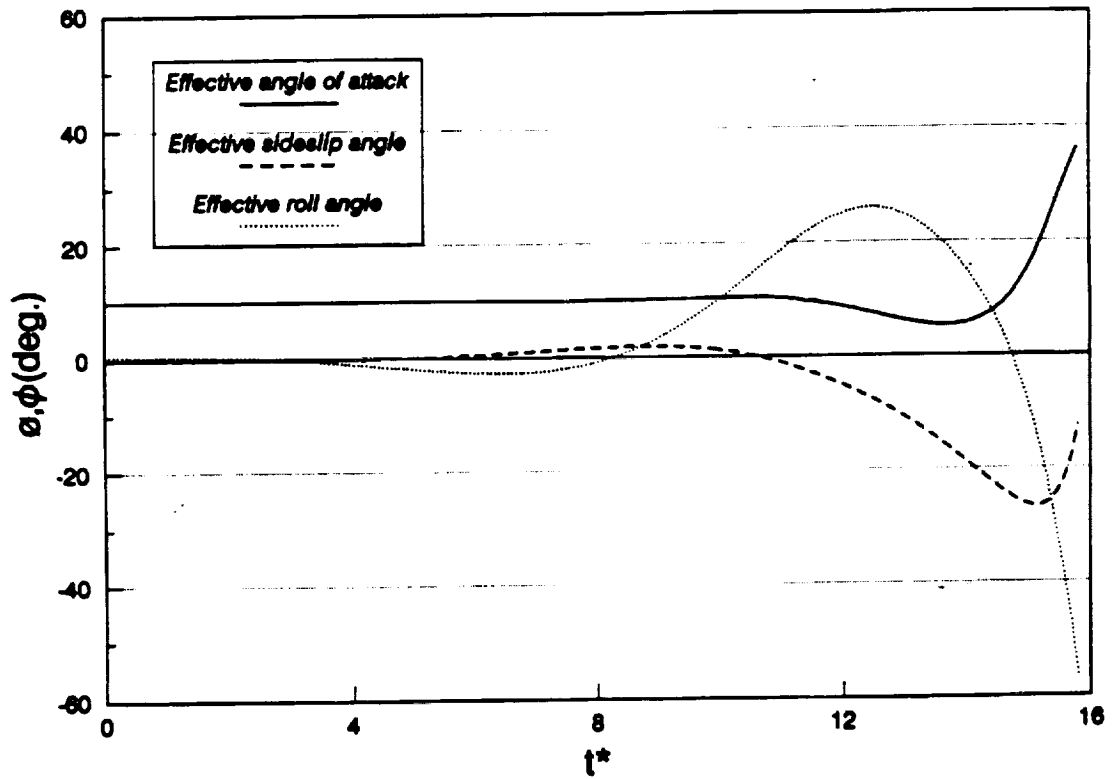


Figure 21(b). Effective Angle of Attack, Yaw Angle and Roll Angle Time History ($\alpha=10^\circ$, $\beta=0^\circ$, $\epsilon=5^\circ$, $\delta=0\%$)

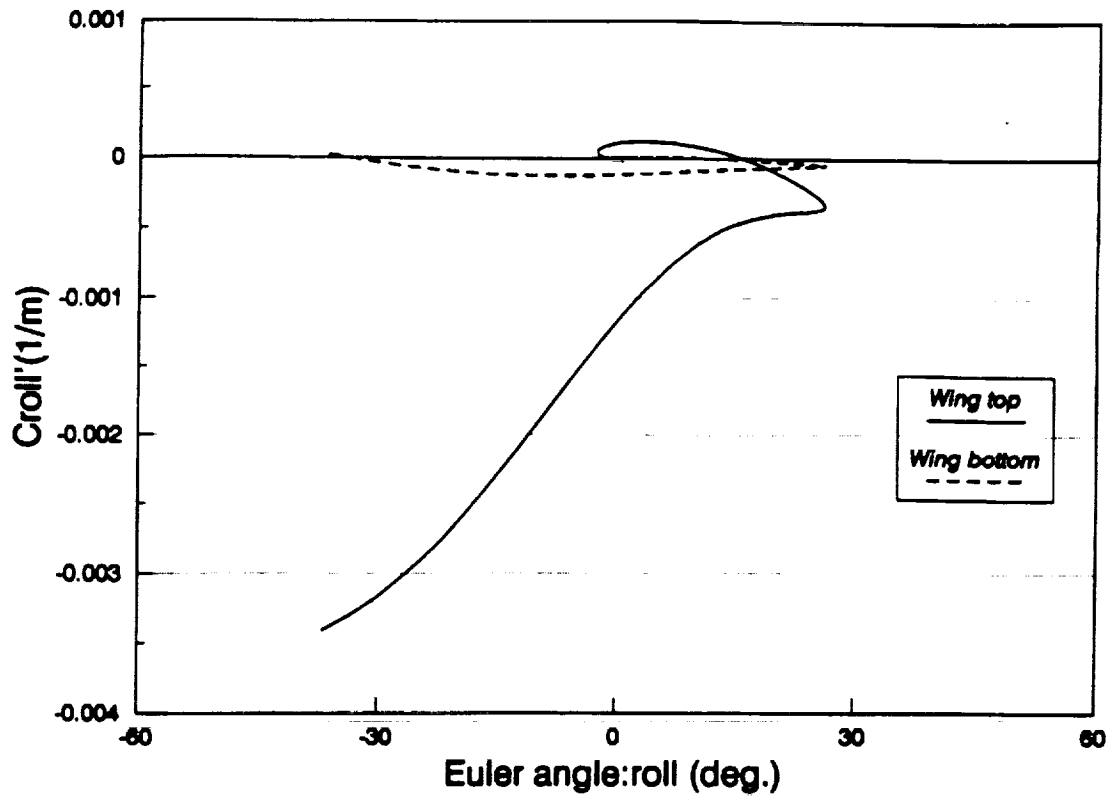


Figure 22(a). Top and Bottom Sectional Roll Coefficient as a Function of Roll Angle ($\alpha = 10^\circ$, $\beta = 0^\circ$, $\epsilon = 5^\circ$, $\delta = 0\%$)

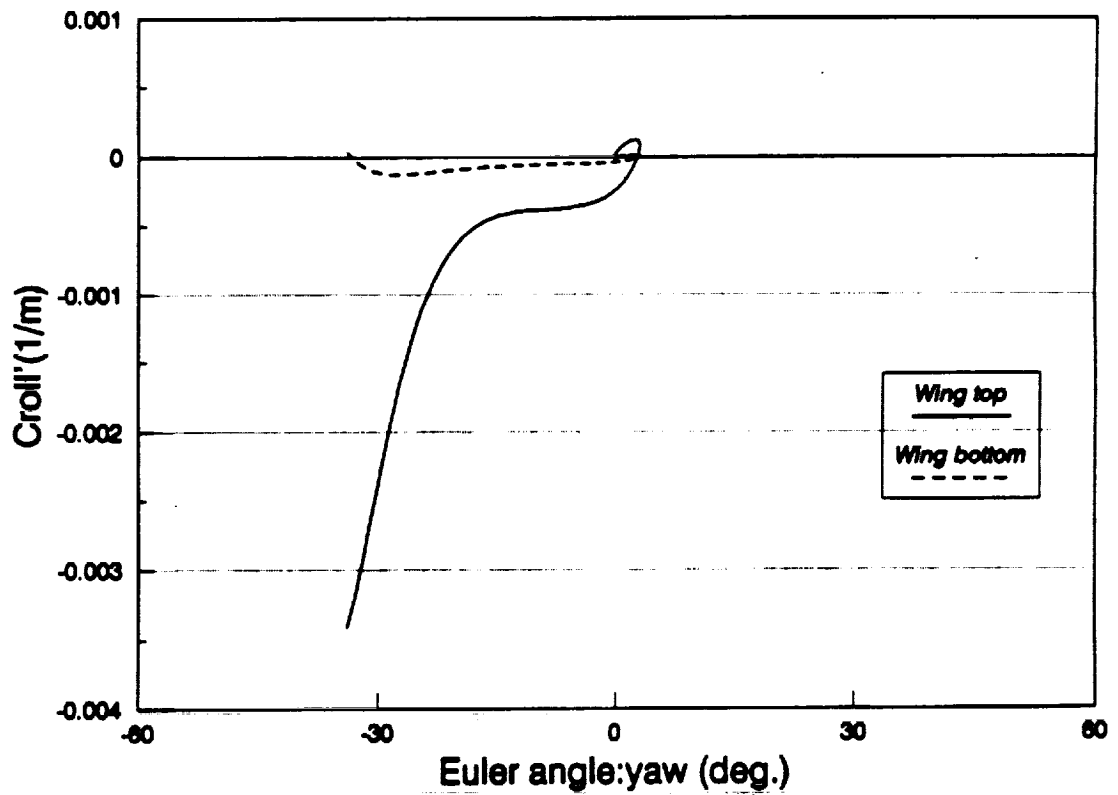


Figure 22(b). Top and Bottom Sectional Roll Coefficient as a Function of Yaw Angle ($\alpha = 10^\circ$, $\beta = 0^\circ$, $\epsilon = 5^\circ$, $\delta = 0\%$)

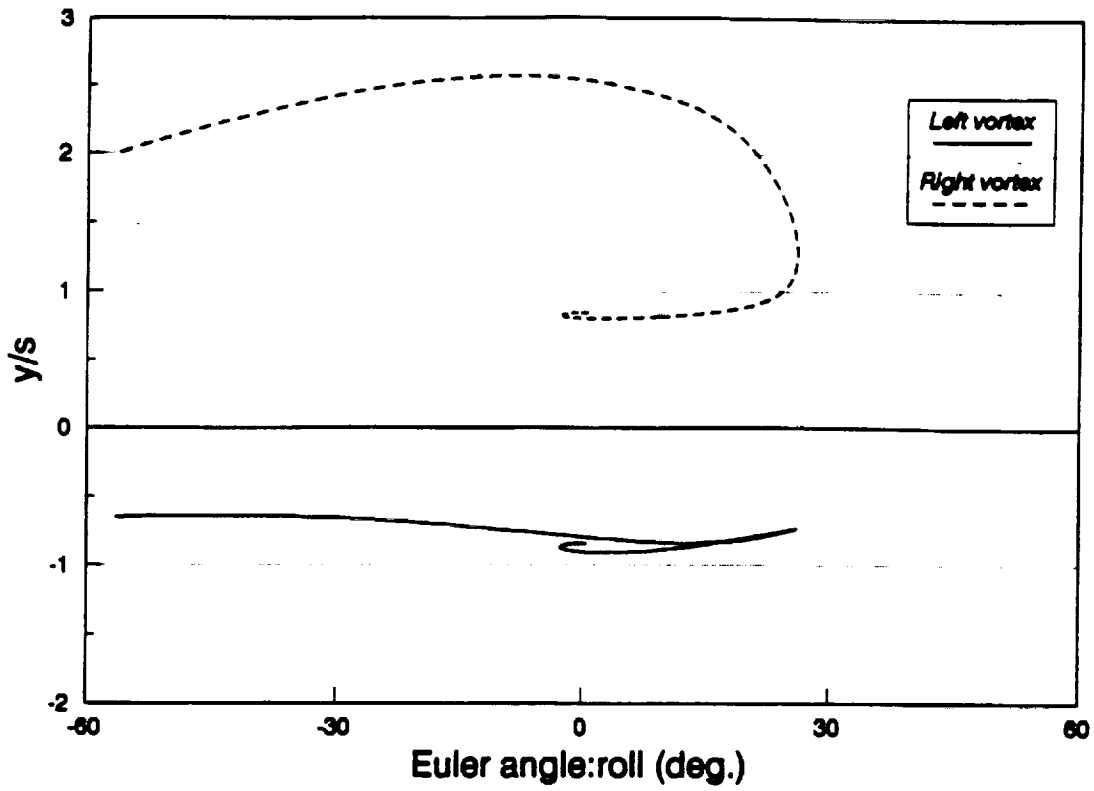


Figure 23(a). Spanwise Vortex Position as a Function of Roll Angle ($\alpha=10^\circ$, $\beta=0^\circ$, $\epsilon=5^\circ$, $\delta=0\%$)

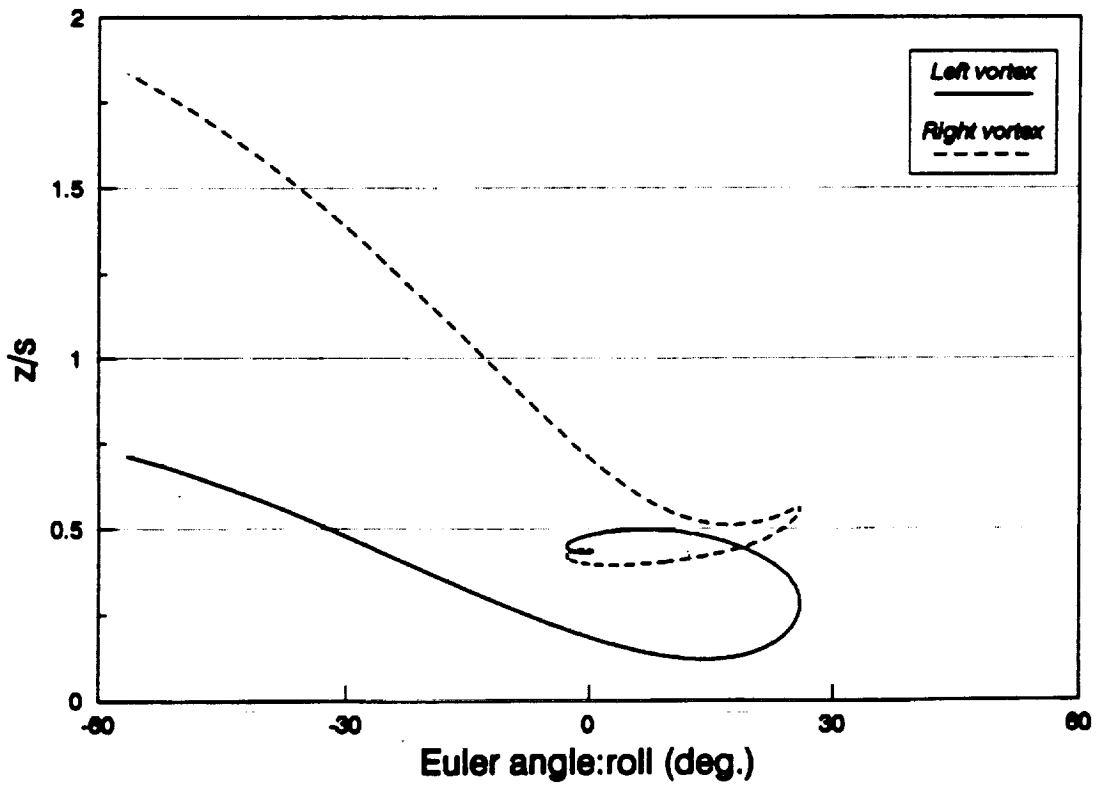


Figure 23(b). Normal Vortex Position as a Function of Roll Angle ($\alpha=10^\circ$, $\beta=0^\circ$, $\epsilon=5^\circ$, $\delta=0\%$)

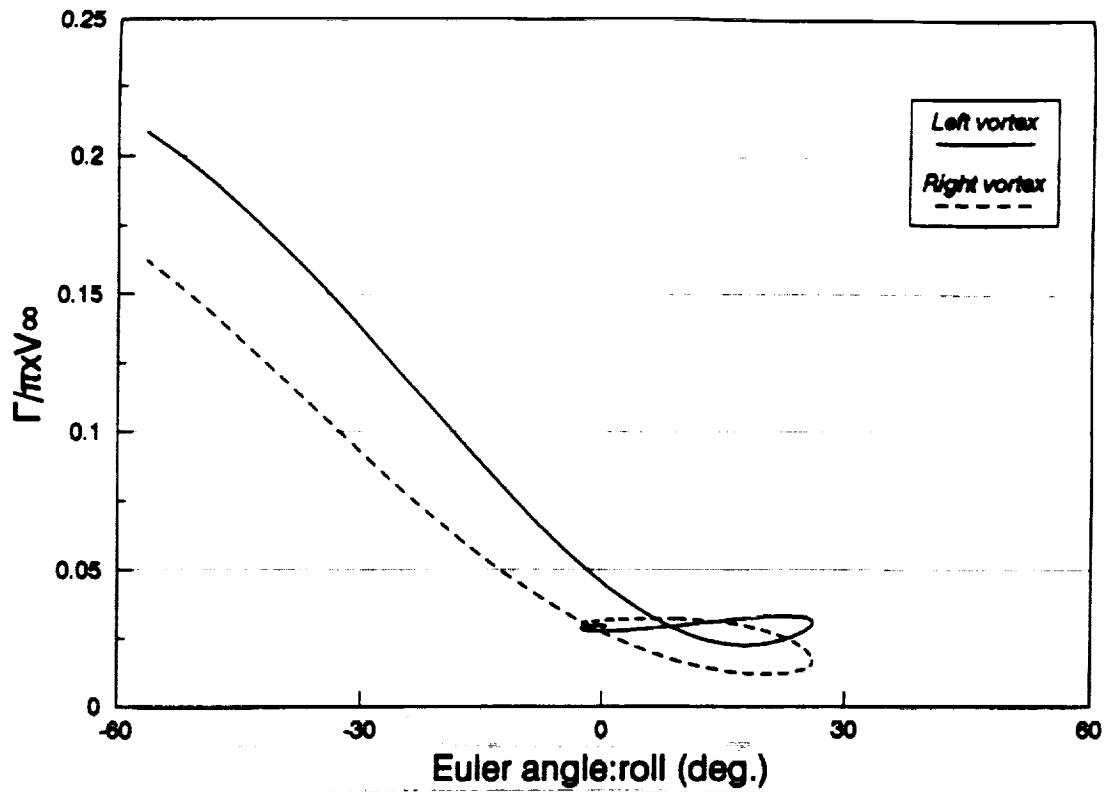


Figure 23(c). Unsteady Vortex Strength as a Function of Roll Angle ($\alpha=10^\circ$, $\beta=0^\circ$, $\epsilon=5^\circ$, $\delta=0\%$)

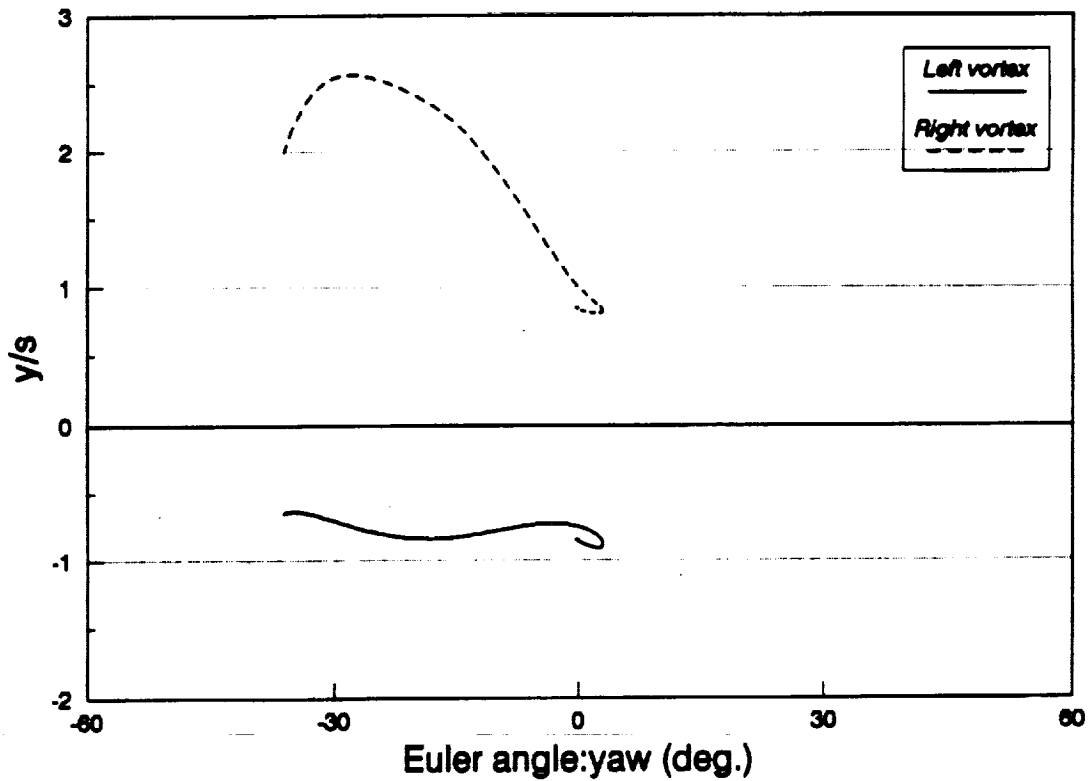


Figure 24(a). Spanwise Vortex Position as a Function of Yaw Angle ($\alpha=10^\circ$, $\beta=0^\circ$, $\epsilon=5^\circ$, $\delta=0\%$)

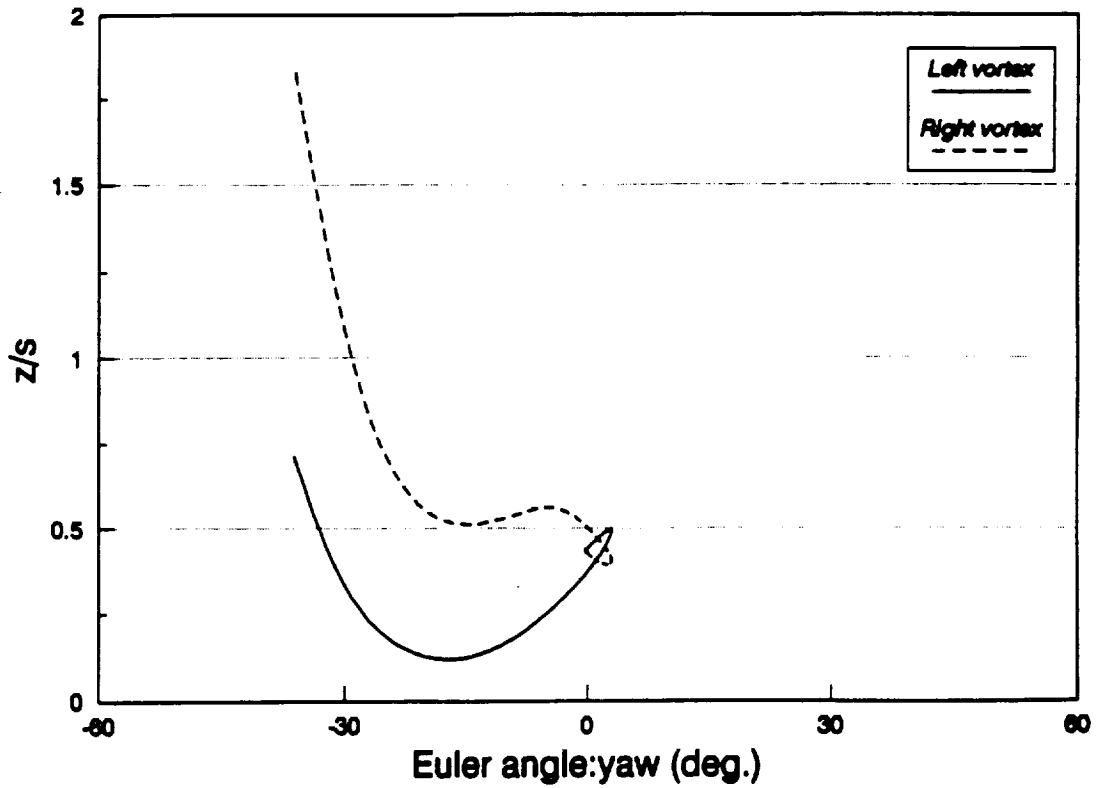


Figure 24(b). Normal Vortex Position as a Function of Yaw Angle ($\alpha=10^\circ$, $\beta=0^\circ$, $\epsilon=5^\circ$, $\delta=0\%$)

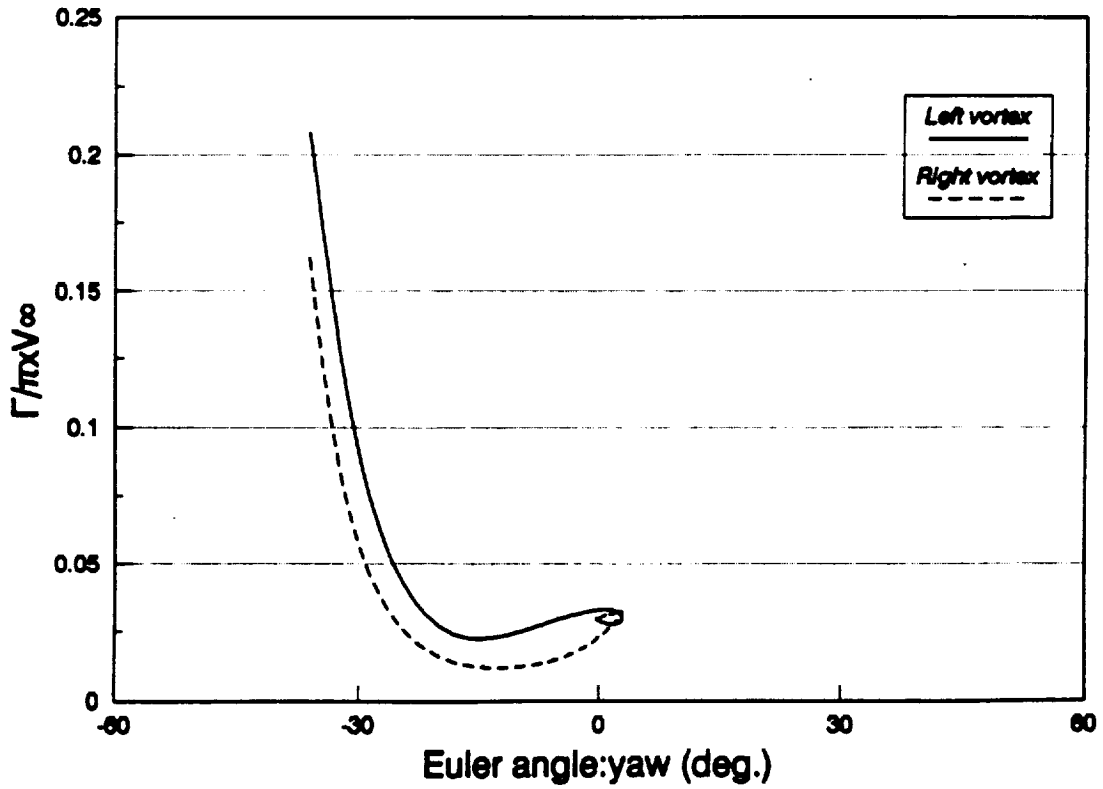


Figure 24(c). Unsteady Vortex Strength as a Function of Yaw Angle ($\alpha=10^\circ$, $\beta=0^\circ$, $\epsilon=5^\circ$, $\delta=0\%$)

